Bioactive Materials 37 (2024) 439–458

Contents lists available at ScienceDirect

Bioactive Materials

journal homepage: www.keaipublishing.com/en/journals/bioactive-materials

Facile and rapid fabrication of a novel 3D-printable, visible light-crosslinkable and bioactive polythiourethane for large-to-massive rotator cuff tendon repair

Xu Zhang [a,b,c], Ke Li [a,b,c], Chenyang Wang [a,b], Ying Rao [a,b], Rocky S. Tuan [a,b,c,e], Dan Michelle Wang [a,b,d,c,e], Dai Fei Elmer Ker [a,b,d,c,e,*]

[a] Institute for Tissue Engineering and Regenerative Medicine, The Chinese University of Hong Kong, New Territories, Hong Kong SAR, China
[b] School of Biomedical Sciences, Faculty of Medicine, The Chinese University of Hong Kong, New Territories, Hong Kong SAR, China
[c] Center for Neuromusculoskeletal Restorative Medicine, Hong Kong Science Park, Hong Kong SAR, China
[d] Ministry of Education Key Laboratory for Regenerative Medicine, School of Biomedical Sciences, Faculty of Medicine, The Chinese University of Hong Kong, New Territories, Hong Kong SAR, China
[e] Department of Orthopaedics and Traumatology, Faculty of Medicine, The Chinese University of Hong Kong, New Territories, Hong Kong SAR, China

ARTICLE INFO

Keywords:
Photo-crosslinkable biomaterials
Polyurethane
Click reactions
3D-printing
Growth factors
Rotator cuff tendon tissue engineering

ABSTRACT

Facile and rapid 3D fabrication of strong, bioactive materials can address challenges that impede repair of large-to-massive rotator cuff tears including personalized grafts, limited mechanical support, and inadequate tissue regeneration. Herein, we developed a facile and rapid methodology that generates visible light-crosslinkable polythiourethane (PHT) pre-polymer resin (~30 min at room temperature), yielding 3D-printable scaffolds with tendon-like mechanical attributes capable of delivering tenogenic bioactive factors. *Ex vivo* characterization confirmed successful fabrication, robust human supraspinatus tendon (SST)-like tensile properties (strength: 23 MPa, modulus: 459 MPa, at least 10,000 physiological loading cycles without failure), excellent suture retention (8.62-fold lower than acellular dermal matrix (ADM)-based clinical graft), slow degradation, and controlled release of fibroblast growth factor-2 (FGF-2) and transforming growth factor-β3 (TGF-β3). *In vitro* studies showed cytocompatibility and growth factor-mediated tenogenic-like differentiation of mesenchymal stem cells. *In vivo* studies demonstrated biocompatibility (3-week mouse subcutaneous implantation) and ability of growth factor-containing scaffolds to notably regenerate at least 1-cm of tendon with native-like biomechanical attributes as uninjured shoulder (8-week, large-to-massive 1-cm gap rabbit rotator cuff injury). This study demonstrates use of a 3D-printable, strong, and bioactive material to provide mechanical support and pro-regenerative cues for challenging injuries such as large-to-massive rotator cuff tears.

1. Introduction

Severe tendon injuries such as large-to-massive rotator cuff tears are challenging to repair due to the simultaneous requirements to withstand loading forces necessary for joint movement as well as enhance healing for restoring native tissue structure, often requiring complex fabrication approaches to develop mechanically strong and bioactive grafts. Tendon injuries can occur as a result of either acute trauma or chronic overuse in a wide demographic range that includes athletes, manual laborers, and the elderly [1–3]. The significance of such injuries is best appreciated from a broad survey of 3246 muscle-tendon-bone defects in 2823 patients [4]. This study showed that a majority (35%) of injuries occurred in the tendon midsubstance [4]. If left unaddressed, such tendon ruptures can pathologically progress into chronic multi-tissue injuries that include bone loss and skeletal muscle fatty degeneration [1–3,5,6]. Although rotator cuff surgeries have been estimated to save the United States economy approximately US$ 3.44 billion annually [7], bibliometric analyses [8,9] indicate that advances in biomaterial scaffolds are still being actively pursued, with existing tendon scaffolds possessing their own inherent advantages and disadvantages [10]. Therefore, there

Peer review under responsibility of KeAi Communications Co., Ltd.
* Corresponding author. Room 425D, Lo Kwee-Seong Integrated Biomedical Sciences Building, Area 39, The Chinese University of Hong Kong, Hong Kong SAR, China.
E-mail address: elmerker@cuhk.edu.hk (D.F.E. Ker).

https://doi.org/10.1016/j.bioactmat.2024.03.036
Received 8 March 2024; Received in revised form 29 March 2024; Accepted 29 March 2024
Available online 25 April 2024

exists a strong impetus to improve existing biomaterial performance.

In this regard, key biomaterial specifications including mechanical properties, biological activity, and manufacturability should be considered. From a biomechanical perspective, tendons such as human SST have high mechanical attributes (tensile strength: 4–22 MPa, tensile modulus: 218–592 MPa [11,12]), which is crucial for efficient transmission of muscle contractile force to bone. Indeed, mechanical attributes such as subpar tendon stiffness have been shown to negatively impact the efficiency of musculoskeletal movement [13] while inadequate tensile strength [14] or poor suture retention [15] may predispose a tendon to failure even after surgical repair. From a biological perspective, tendons often do not fully regenerate and instead heal by fibrovascular scar tissue formation [6,16]. Given that tendon tissue structure, such as collagen fiber crimping, is important for tendon's mechanical response [17], the loss of highly aligned, load-bearing collagen fibers results in mechanically weakened tissue, reducing tendon's tensile strength by as much as 70% [18]. In large-to-massive rotator cuff tears, poor mechanical integrity coupled with inadequate biologic healing is responsible for a high re-tear rate (up to 91%) even after surgical repair [19,20]. From a manufacturability perspective, advanced fabrication techniques that facilitate facile and rapid production of patient-specific grafts are also desired. Rotator cuff tears may differ not only in the magnitude of their tear size but also their morphological shape. For example, rotator cuff tears can be classified as crescent-shaped, reverse L-shaped, L-shaped, trapezoidal-shaped, and massive full-thickness tears [21]. These morphological differences are important as they can differentially impact rotator cuff kinematics such as humeral internal rotation and superior translation [22] as well as patient outcomes in terms of pain and shoulder function [23]. Although customized rotator cuff grafts are not commercially available, it is common practice for orthopaedic surgeons to personalize a graft for a particular lesion size and shape [24], highlighting the need for rapid on-demand, low-volume production of customized grafts. Together, rapid and facile production of mechanically robust and bioactive tendon-like materials is highly desirable to address biological and mechanical deficits present in rotator cuff injuries as well as facilitate personalized graft fabrication for improving patient outcomes.

To address these key issues, we developed a facile method for fabricating a mechanically robust, slow degrading, and bioactive, 3D-printable polythiourethane elastomer known as PHT polymer and performed chemical, mechanical, and biological characterization to demonstrate its ability to restore native tendon-like biomechanical function and enhance tissue healing (Scheme 1). Facile synthesis of PHT polymer is attained by 30-min mixing of pentaerythritol tetrakis (3-mercaptopropionate) (P), hexamethylene diisocyanate (H), and trimethylolpropane triacrylate (T) under ambient, room temperature conditions followed by visible light 3D-printing and heat curing, resulting in highly crosslinked, polythiourethane networks. *Ex vivo*, 3D-printable PHT polymer achieved robust tendon-like mechanical properties, including the ability to sustain 10,000 cycles of physiologic loading (0.2–3 MPa per cycle), exhibited slow degradation under alkaline and acidic conditions, and showed sustained growth factor release, specifically tendon-promoting FGF-2 and TGF-β3. *In vitro*, PHT polymer exhibited minimal cytotoxicity, supported cell attachment, and facilitated tendon-like differentiation. *In vivo*, PHT polymer showed biocompatibility in a mouse subcutaneous implantation model and restored rotator cuff biomechanical function and enhanced tissue healing in a rabbit large-to-massive injury model. In the injury model, implantation with PHT polymer containing a relatively low dose of FGF-2 and TGF-β3 demonstrated higher ultimate load and similar stiffness as non-operated controls, and about 1-cm tendon regeneration was observed. These observed effects support the likelihood of achieving successful tendon repair outcomes using facilely produced PHT constructs.

2. Results

In this study, PHT polymer was first synthesized in a two-step

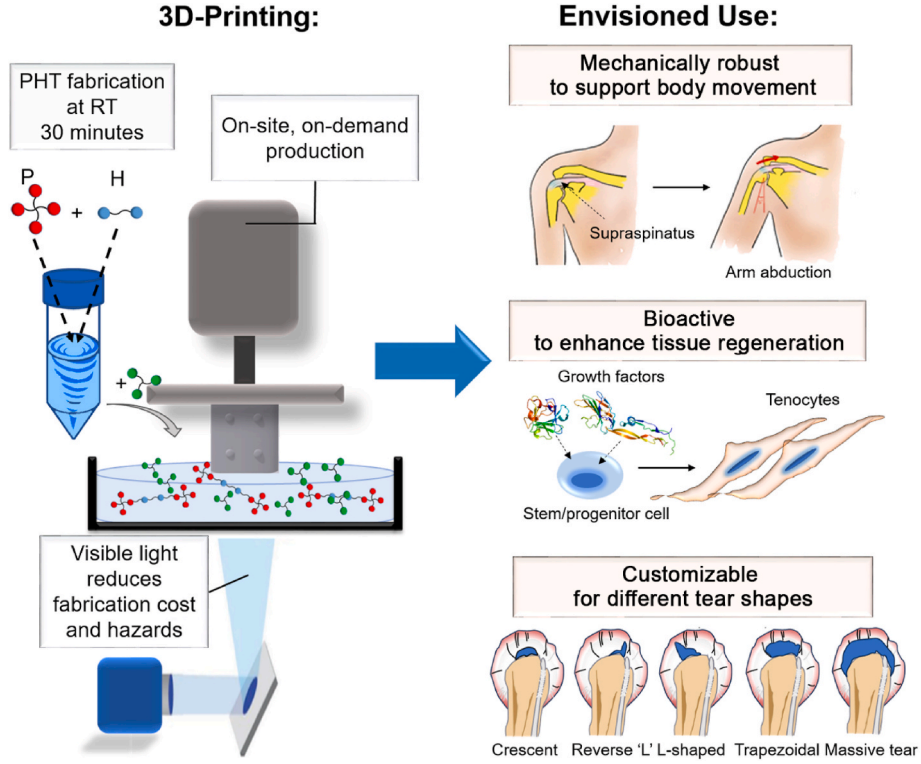

Scheme 1. Facile and rapid fabrication of polythiourethane (PHT) polymer is attainable at room temperature via a 30-min reaction, yielding a pre-polymer resin suitable for visible light-mediated 3D-printing. This novel PHT polymer exhibits robust mechanical properties to support joint movement, is capable of delivering tenogenic bioactive factors to enhance tissue regeneration, and can be customizable for different patient tear morphologies.

reaction and subsequently characterized *ex vivo* (FTIR, mechanical, degradation, and growth factor retention/release studies), *in vitro* (cell viability, cell attachment, and tenogenic differentiation assays), and *in vivo* (mouse subcutaneous and rabbit large-to-massive rotator cuff defect models) (Fig. 1a).

2.1. Synthesis and ex vivo chemical characterization of PHT polymer and 3D-printed PHT scaffold

2.1.1. Two-step fabrication of PHT polymer and chemical characterization of PHT polymer by FTIR

PHT polymer was synthesized from P, H and T with a desired ratio through a facile two-step fabrication process (Fig. 1b). In the first step, PH pre-polymer was synthesized by simple mixing of P and H with the addition of a small amount of catalyst using a vortex mixer. In the second step, the PH pre-polymer was mixed and reacted with T under visible light exposure to form PHT polymer (Fig. 1b). The pre-polymer resin can be prepared via simple mixing in 30 min or less and subsequently 3D-fabricated under ambient, room temperature conditions.

To monitor the fabrication of PHT polymer, Fourier transformed infrared (FTIR) spectroscopy was used to characterize the chemical reactions among P, H, and T monomers as well as under the presence of increasing visible light exposure (Fig. 1c and Fig. S1). The FTIR spectra of P/H, P/T and H/T indicated that chemical reactions occurred between P (-SH) and H (-N═C═O) as well as P (-SH) and T (-CH═CH_2) to form thiocarbamate and alkyl sulfide bonds, respectively, but not between H and T (Fig. S2). Formation of thiocarbamate is evident from the complete loss of signals at 2220-2280 cm^{-1} (-N═C═O) and reduced signals at 2550-2600 cm^{-1} (-SH) (Fig. 1c), which were attributed to stretching vibrations of both isocyanate and of thiol groups [25–27], as well as the appearance of signals around 1176-1299 cm^{-1} and 3359 cm^{-1} (Fig. 1c), which were attributed to stretching vibrations of carbamate carbonyl (-C═O) groups and carbamate amine (-NH) groups undergoing hydrogen bonding with carbonyl groups [25–27]. The complete loss of the isocyanate signal indicated complete reaction of H [25] (Fig. 1c). Formation of alkyl sulfide bonds is evident from loss of the aforementioned thiol (-SH) as well as acrylate alkene (-CH═CH_2) signals (Fig. 1d). FTIR spectra of PHT pre-polymer under increased visible light exposure indicated increased reactions between the thiol group of PH pre-polymer and the acrylate alkene group of the T, which were reflected within two regions-of-interest (Fig. 1e and f). These two regions-of-interests include signals at 809 and 2566 cm^{-1}, which were attributed to the stretching vibrations of acrylate alkene (-CH═CH_2) and thiol (-SH) respectively. To compare these signals, the wave number at 780 ± 20 cm^{-1}, which was attributed to the bending mode of –CH [28] was used as an invariant peak for normalization [25]. In such comparisons, the ratio of the peak values at 809 ± 5 (-CH═CH_2)/780 ± 5 (-CH), as well as 2566 ± 5 (-SH)/780 ± 5 (-CH) were gradually decreased with increased visible light exposure, indicating visible light-induced photo-crosslinking between PH pre-polymer and T (Fig. 1e and f). Together, this facile mixing method demonstrated expected formation of polythiourethane networks via a combination of chemical- and visible light-induced photo-crosslinking for rapid production of photo-crosslinkable 3D-printing resins.

2.1.2. 3D-printing properties of PHT polymer

To determine the 3D-printability of PHT polymer, we designed and 3D-fabricated a tendon sheath-like scaffold with wavy topography and semi-spherical physical features followed by comparative assessment of 3D-printing fidelity via digital photographs and reconstructed micro-computed tomography (microCT) images (Fig. 1g). The computer-aided design (CAD) model was engineered to mimic aspects of tendon structure and architecture such as its anisotropic nature and crimped tendon fibers [29] with the semi-spherical physical features as fiduciary markers to facilitate *in vivo* suturing (Fig. 1g). Digital photographs and reconstructed microCT images of 3D-printed PHT scaffolds showed good concurrence of scaffold morphology and porosity with the computer-aided design, demonstrating the pre-polymer's resin fidelity for 3D-printing fabrication (Fig. 1g). Also, photoelastic stress analysis of 3D-printed PHT scaffolds showed that 3D-fabricated specimens did not contain any internal residual stress following fabrication relative to standard tissue culture plasticware, as evidenced by the lack of induced colour birefringence (Fig. S3). Together, these data showed that PHT polymer was 3D-printable using visible light with high fidelity.

2.2. Ex vivo mechanical characterization of PHT polymer and 3D-printed PHT scaffold

To determine the mechanical properties of PHT polymer, static tensile, cyclic tensile, static creep tensile, and suture retention tests were performed with PHT polymer post-heat cured at 150 °C for 2, 4 and 8 h separately (Fig. 2). Heat curing of PHT polymers was performed to increase tensile properties of the polymers [25].

2.2.1. Static tensile properties

PHT polymers with 2-, 4- and 8-h of heat curing were mechanically assessed following the guidelines in American Society for Testing and Materials (ASTM) methods D638-10 (Tensile properties of plastics). With increased heat curing times, ultimate tensile stress increased from 18.2 ± 0.49 MPa (2h-PHT) to 27.5 ± 0.41 MPa (8h-PHT) (Fig. 2a). Similarly, the tensile modulus increased from 184.8 ± 7.91 MPa (2h-PHT) to 843.7 ± 31.97 MPa (8h-PHT) (Fig. 2a). Conversely, the ultimate strain decreased with increased post heat curing time, with 4h-PHT and 8h-PHT showing physiologically relevant strains of 10–20% (Fig. 2a). Also, 2h-, 4h-, and 8h-PHT showed a total work-to-failure of around 0.15 J and tensile toughness of around 3 MPa (Fig. 2a). In addition, when tensile strength and tensile modulus were normalized using their respective tensile attribute for human supraspinatus tendon (SST), 4h-PHT polymer was identified to be most SST-like relative to the clinically used rotator cuff patches and recently developed biomaterial scaffolds (Fig. 2a and Table S1) [30–33]. Together, these data demonstrated that PHT polymer exhibited heat curing dependent tensile properties that were reminiscent of human SST tendon.

2.2.2. Cyclic tensile properties

To determine the mechanical robustness of PHT polymer, PHT polymers with 2-, 4- and 8-h of heat curing were mechanically assessed following the guidelines in ASTM methods D7791-12 (Uniaxial fatigue properties of plastics) (Fig. 2b). A physiologically relevant tension loading regimen of 0.2–3 MPa per cycle was chosen as this mimicked 75% of the failure stress observed for human SST in Itoi et al. [11,25]. All samples sustained at least 10,000 loading cycles of 0.2–3 MPa tensile stress without failure (Fig. 2b). The maximum strain (%) observed during 10,000 loading cycles were within a physiologically relevant range (less than 3%) for 2h-PHT, 4h-PHT, and 8h-PHT with a relatively consistent dynamic, storage and loss moduli throughout testing (Fig. 2b). Together, these data showed that PHT polymer was mechanically robust and exhibited stable tensile properties during cyclic fatigue testing.

2.2.3. Static creep tensile properties

PHT polymers with 2-, 4- and 8-h of heat curing and a clinically available acellular dermal matrix (ADM; GraftJacket™) were mechanically assessed using a 30-min static creep hold at a physiologically relevant stress of 3 MPa [25] followed by rapid unloading to monitor its recovery performance (Fig. 2c). PHT polymers exhibited decreased creep strain (%) with increased heat curing time. The creep strain of 4h-PHT (2.92 ± 0.12%) and 8h-PHT (0.85 ± 0.03%) were markedly lower than the strain change of ADM (4.90 ± 0.24%). Also, both 4h-PHT and 8h-PHT achieved more than 80% recovery (83.01 ± 1.45% for 4h-PHT, 92.71 ± 4.04% for 8h-PHT) compared to 22.62 ± 2.54% recovery for ADM after a 10-min rest period (Fig. 2c). Together, these data

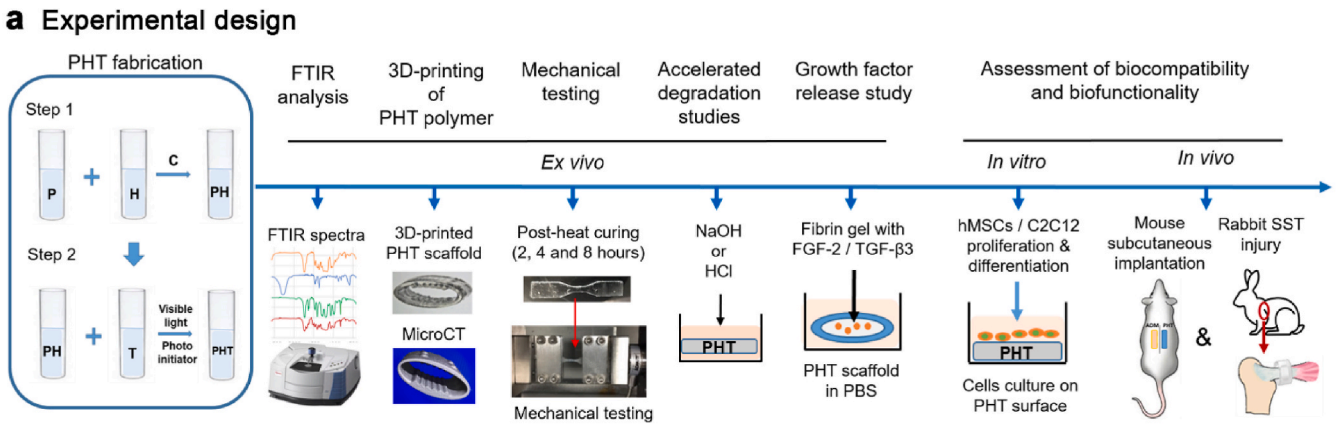

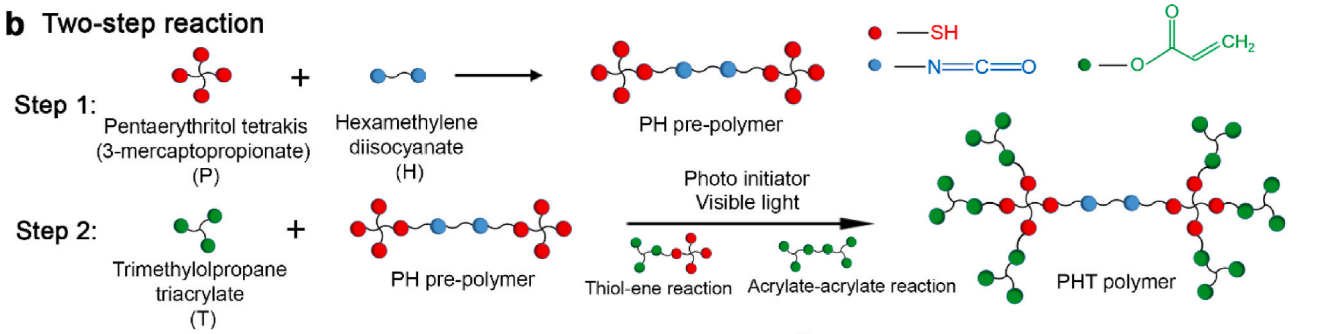

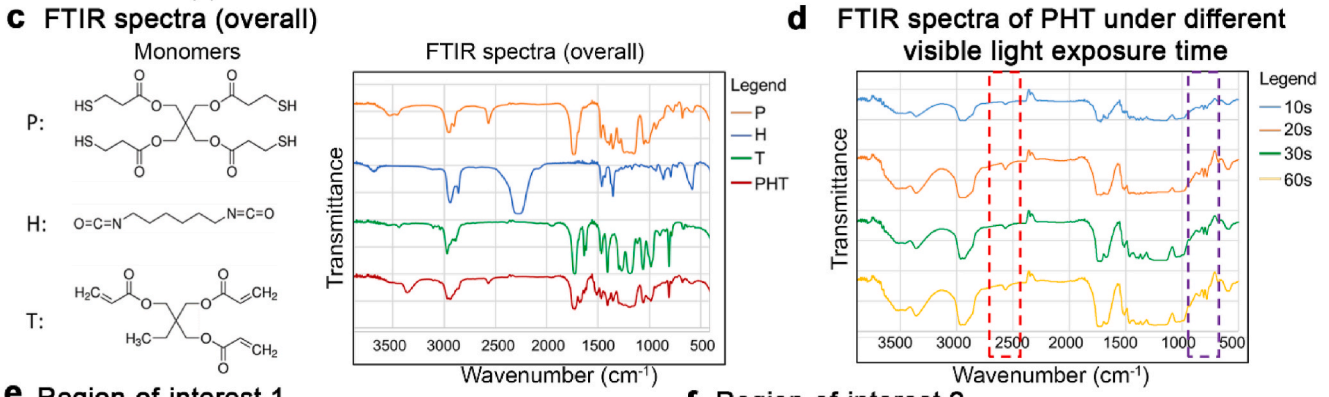

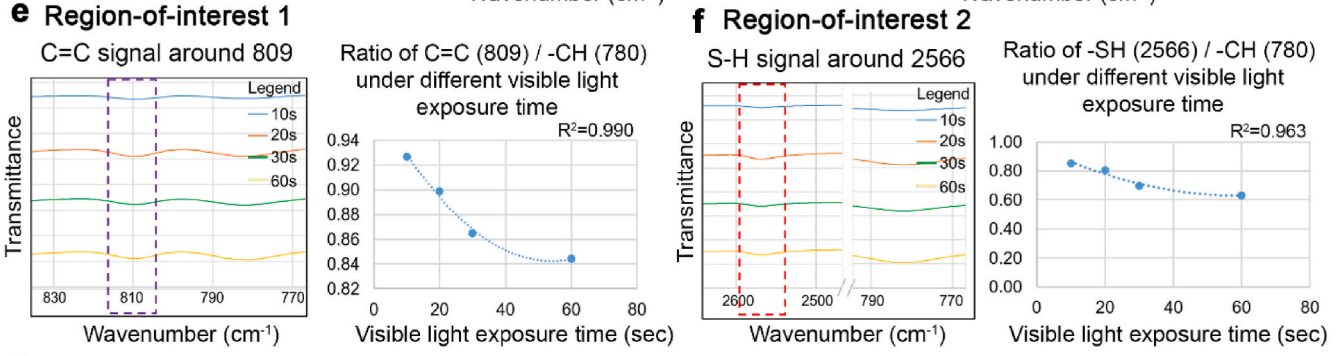

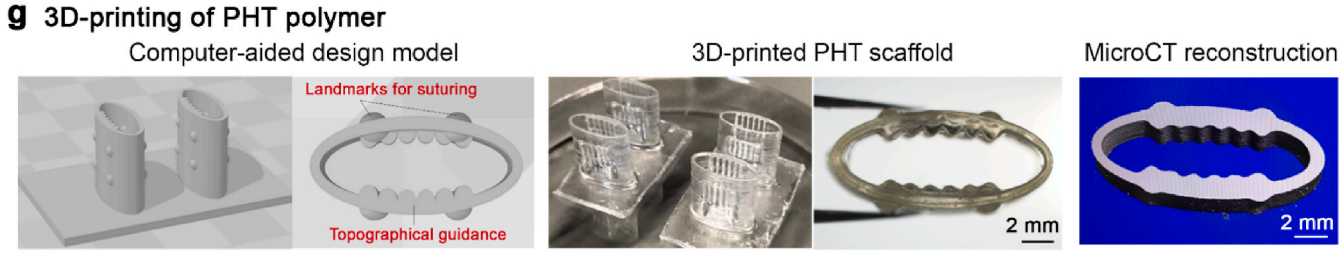

(caption on next page)

Fig. 1. Experimental design and synthesis of PHT polymer. PHT pre-polymer could be rapidly prepared under ambient room temperature conditions for 3D-printing. (a) Experimental design of the whole presented work. (b) Synthesis of PHT polymer via a two-step reaction. (c) FTIR spectra of individual PHT components (P, H and T) and PHT polymer without visible light exposure. (d) FTIR spectra of PHT polymer under different visible light exposure time. Region-of-interest 1 and 2 are indicated by purple and red dashed boxes, respectively. (e) Region-of-interest 1 showed a C═C signal around 809 wavenumber and ratio of C═C (809)/–CH (780) under different visible light exposure time. (f) Region-of-interest 2 showed an S–H signal around 2566 wavenumber and ratio of –SH (2566)/–CH (780) under different visible light exposure time. (g) Computer-aided designed (CAD) model with digital photograph and micro-computed tomography (microCT) reconstruction images of 3D-printed tendon sheath-like PHT scaffold.

showed that PHT polymer exhibited robust mechanical performance in response to time-dependent stress and excellent recovery performance.

2.2.4. Suture retention properties

Suture tear through of tendon is the most frequent mode of failure in rotator cuff repair [25,34,35] and therefore vital for ensuring repair construct integrity post-surgery. To determine the suture retention properties of PHT polymer, ADM and 3D-printed PHT scaffold fabricated from 4h-PHT, which best mechanically mimics human SST, were assessed by measuring suture migration during load-to-failure tensile tests (Fig. 2d). At 15 N during load-to-failure, 3D-printed scaffold fabricated using 4h-PHT exhibited only 0.4 ± 0.03 mm suture migration, which was 8.62-fold lower than ADM (3.45 ± 0.21 mm) (Fig. 2d). Together, these data demonstrated that 3D-printed PHT scaffold exhibited excellent suture retention relative to ADM.

2.2.5. Tensile properties of 3D-printed PHT scaffold

To determine the tensile properties of mock repaired tendon constructs, ADM and 3D-printed PHT scaffold fabricated from 4h-PHT were mechanically assessed by ultimate load and total-work-to-failure during load-to-failure tensile tests (Fig. 2e). 3D-printed PHT scaffold exhibited a similar ultimate load (54.69 ± 2.26 N) as ADM (56.68 ± 1.38 N) but showed two-fold higher total work-to-failure (3D-printed PHT scaffold: 0.24 ± 0.02 J, ADM: 0.12 ± 0.02 J) (Fig. 2e). Together, these data demonstrated that 3D-printed PHT scaffold exhibited excellent tensile properties relative to ADM.

2.2.6. Summary of 3D-printed PHT scaffold mechanical properties

In summary, PHT polymers showed increased mechanical characteristics with increased heat curing. In particular, 4h-PHT polymer demonstrated competent biomechanical properties including human SST-like tensile strength (23.3 ± 0.50 MPa) and tensile modulus (459.4 ± 17.13 MPa), high mechanical robustness vis-à-vis withstanding at least 10,000 cycles of physiological loading without failure, physiologically relevant time-dependent mechanical response and recovery, and superior suture retention as well as tensile attributes relative to clinically available ADM. On the basis of these findings, 4h-PHT polymer was used to fabricate 3D-printed PHT scaffold for subsequent degradation and swelling assays, growth factor retention/release experiments, as well as *in vitro* and *in vivo* studies.

2.3. Ex vivo degradation and swelling studies of PHT polymer

Degradation and swelling studies were performed to determine the physical integrity of PHT polymers and ADM under normal (neutral) or pathologic (acidic or alkaline or oxidizing) physiological conditions such as chronic wound environments and foreign body reaction to implanted materials (Fig. 3a). In swelling studies, PHT polymer samples were incubated under neutral (Hank's buffered salt solution/HBSS), alkaline (5 N NaOH) and acidic (1 N hydrochloric acid/HCl) condition for 4 h and exhibited little-to-no swelling under neutral, alkaline, and acidic conditions (Fig. 3b). In accelerated degradation studies, PHT polymer and ADM samples were incubated under alkaline (5 N sodium hydroxide/NaOH) and acidic (2 N HCl) conditions for 5 days as well as oxidizing (30% hydrogen peroxide/H_2O_2) conditions for 1 week, which resulted in differential mass loss (Fig. 3c). Under acidic and oxidizing conditions, both PHT polymers and ADM exhibited little-to-no mass loss whereas under alkaline conditions, PHT polymers and ADM exhibited ~69% and 100% mass loss, respectively (Fig. 3c). Static tensile testing of PHT polymers and ADM which showed little-to-no degradation following 5-days incubation in 2 N HCl exhibited similar changes in tensile properties when normalized to pristine samples (Fig. 3d). Together, these data showed that PHT polymers degraded more slowly compared to commercially available ADM graft under physiologically relevant, simulated body conditions.

2.4. Ex vivo growth factor retention/release from 3D-printed PHT scaffold

An essential characteristic of a biocompatible tendon tissue engineered scaffold is its ability to retain and release relevant bioactive factors, e.g., FGF-2 and TGF-βs, which are known to bind to extracellular matrix molecules such as fibrinogen [36,37]. To assess the retention/-release profile of tendon-promoting FGF-2 and TGF-β3 [1,29,38–40] from 3D-printed PHT scaffolds containing fibrin hydrogel, enzyme-linked immunosorbent assay (ELISA) kits were used to monitor growth factor release for up to 2 weeks (Fig. 4). To account for potential confounding variables such as growth factor half-life [41], masking of antibody recognition sites due to growth factor-soluble extracellular matrix interactions, etc., retention/release studies were limited to 6- and 14-days for FGF-2 [42] and TGF-β3 [43,44], respectively, and terminologies such as 'ELISA-detectable FGF-2' or 'ELISA-detectable TGF-β3' values were reported. For FGF-2, ELISA-detectable FGF-2 showed a burst release with the highest concentration of 4.285 ± 0.795 ng/mL during the initial 8 h and a steady release from day 2 until day 6 (Fig. 4a). The calculated cumulative mass and percentage of ELISA-detectable FGF-2 released was 61.56 ng and 2.03 % after 6-days (Fig. 4a). For TGF-β3, ELISA-detectable TGF-β3 was gradually released from the fibrin gel, and reached a peak concentration of 24.865 ± 0.785 ng/mL at day 10 (Fig. 4b). The calculated cumulative mass and cumulative percentage of ELISA-detectable TGF-β3 released was 309.5 ng and 51.11 % after 14-days (Fig. 4b). Together, these data showed controlled, sustained release of FGF-2 and TGF-β3 from 3D-printed PHT scaffolds containing fibrin hydrogel.

2.5. In vitro biocharacterization of 3D-printed PHT scaffold

2.5.1. Cell attachment and cell viability assay on PHT polymer

To assess the ability of PHT polymer to support cell attachment and viability, C2C12 cells and human mesenchymal stem cells (hMSCs) were independently cultured on the surface of PHT polymers with 2-, 4- and 8-h of heat curing or 3D-printed PHT scaffolds fabricated from 4h-PHT and subsequently subjected to cell counting, Live/Dead assay, and scanning electron microscopy (SEM) studies (Fig. 5a). C2C12 cells and hMSCs were used as model surrogates of muscle-derived stem/progenitor cells and mesenchymal stem cells, respectively. These cell types have been explored for their potential in cell-based therapeutics for tendon regeneration [39,45]. Cell counting studies at 3-h post-seeding indicated that the cell densities of C2C12 cells and hMSCs remained constant (2h-PHT: 7.31×10^4 cells/cm^2, 4h-PHT: 7.45×10^4 cells/cm^2, 8h-PHT: 8.26×10^4 cells/cm^2) and there was no difference among groups of different heat curing times (Fig. 5b). Live/Dead analysis showed that a majority of C2C12 cells and hMSCs were viable on all PHT polymers with few cell death, compared to the 70% methanol-treated negative controls (Fig. 5c). No obvious difference of cell viability was found among PHT polymers with different heat curing times. SEMstudies

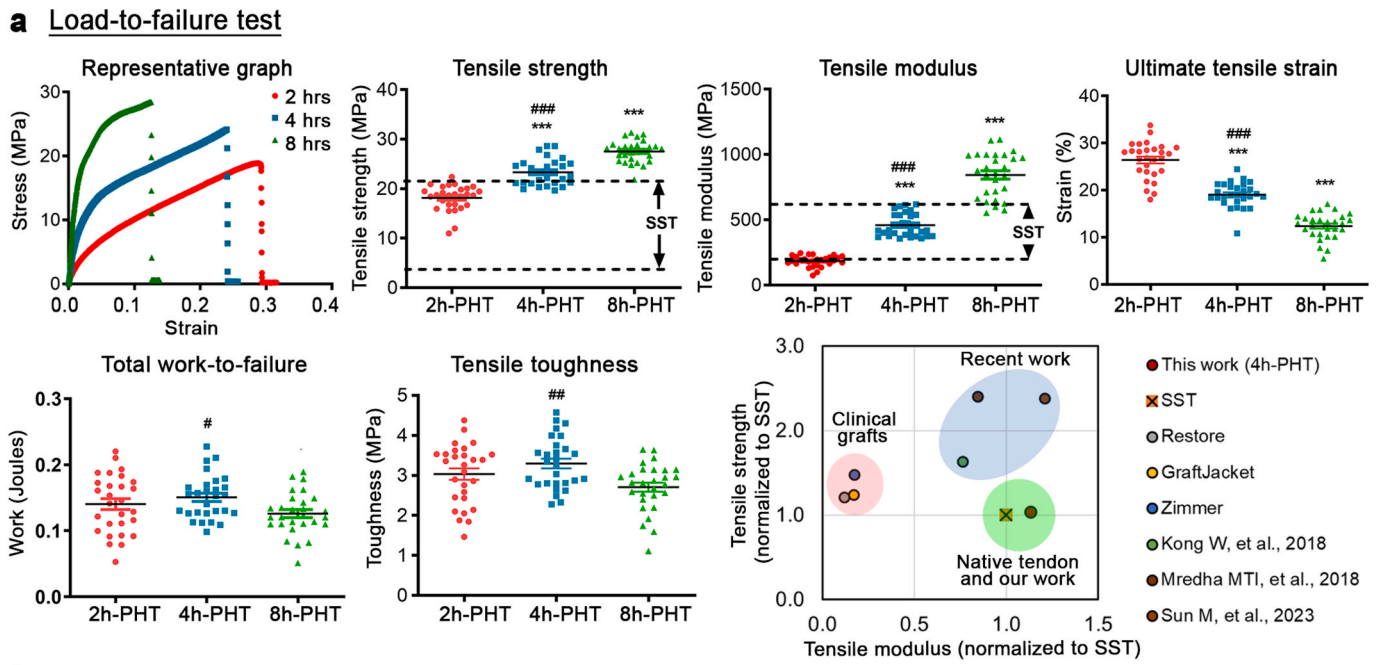

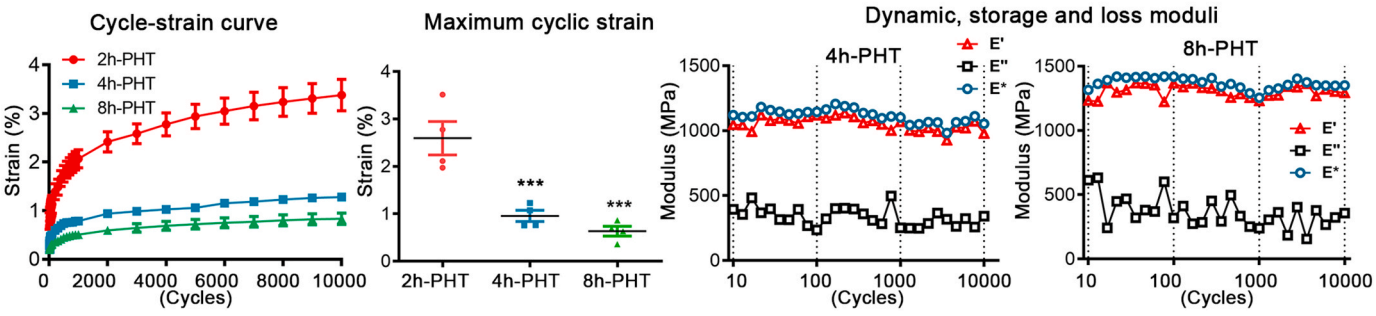

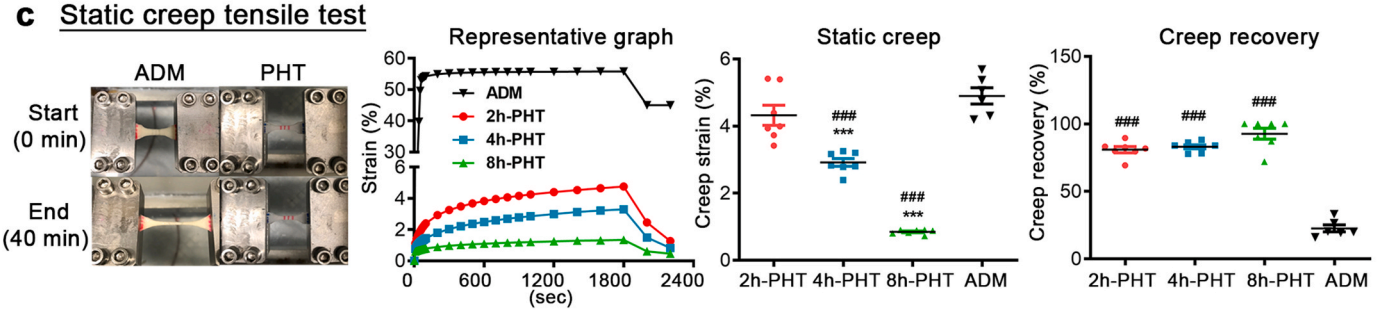

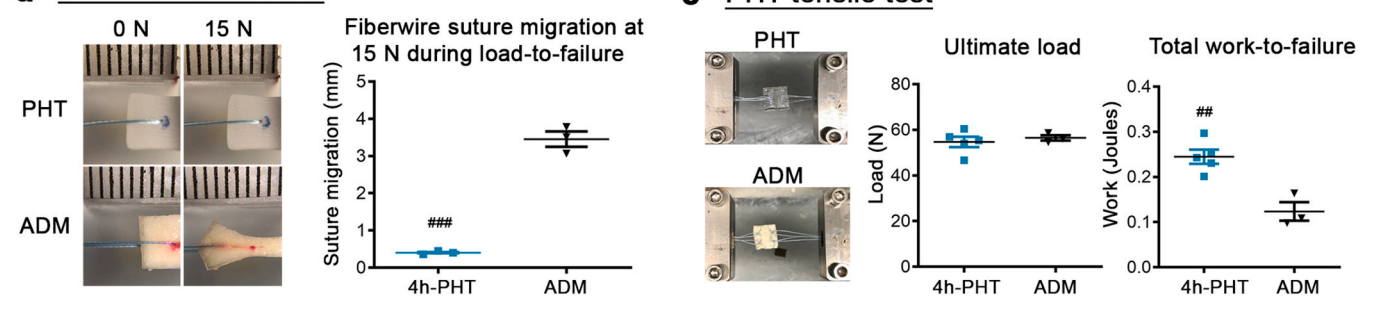

(caption on next page)

Fig. 2. Mechanical properties of PHT polymers and 3D-printed PHT scaffold. PHT polymers and 3D-printed PHT scaffold exhibited mechanically robust, tendon-like properties. (a) Load-to-failure test of PHT polymer post-heat cured for 2, 4 and 8 h separately (n = 28 for each group). Tensile strength, tensile modulus, ultimate strain, total work-to-failure, and toughness were determined. Ashby chart simultaneously comparing the tensile strength and tensile modulus of human supraspinatus tendon (SST) with 4h-PHT, clinical grafts, and recently developed tendon biomaterial scaffolds showed that 4h-PHT was most similar to human SST. ***: $p \leq 0.001$; statistical significance was relative to 2h-PHT. #: $p \leq 0.05$; ##: $p \leq 0.01$; ###: $p \leq 0.001$; statistical significance was relative to 8h-PHT. (b) Cyclic tensile test of PHT polymer post-heat cured for 2, 4 and 8 h separately (10,000 cycles from 0.2 to 3 MPa at 1 Hz, n = 4 for each group). Cycle-strain curve, maximum cyclic strain as well as dynamic, storage and loss moduli were calculated and analyzed. ***: $p \leq 0.001$; statistical significance was relative to 2h-PHT. (c) Static creep tensile testing (3 MPa) of 2h, 4h, and 8h-PHT (n = 7 for each group). Representative images showing the ADM and PHT sample before testing (0 min) and at the end of testing (40 min). Static creep strain (%) and creep recovery (%) were determined. ***: $p \leq 0.001$; statistical significance was relative to 2h-PHT. ###: $p \leq 0.001$; statistical significance was relative to ADM. (d) Suture retention of 4 h post-heat cured PHT polymer and ADM (n = 3 for each group). FiberWire suture migration at 15 N during load-to-failure was calculated for 4h-PHT and ADM. ###: $p \leq 0.001$; statistical significance was relative to ADM. (e) Tensile testing of 3D-printed PHT scaffold post-heat cured for 4 h and ADM (4h-PHT: n = 5, ADM: n = 3). Ultimate load and total work-to-failure were determined for 4h-PHT and ADM. Error bars indicate standard error of mean.

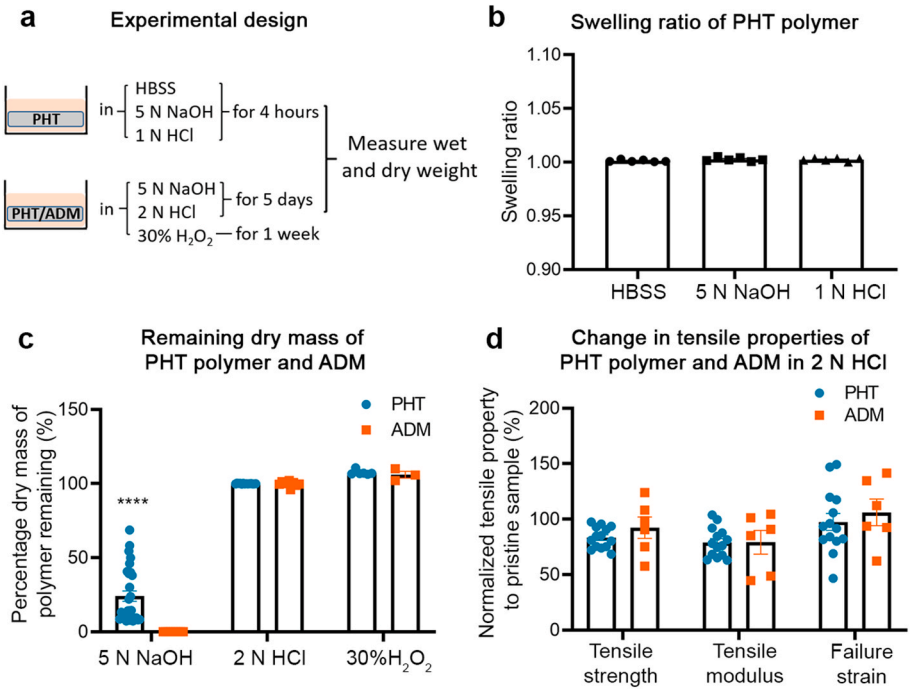

Fig. 3. Accelerated degradation and swelling studies of PHT polymer. PHT polymer degraded slowly under alkaline, acidic, and oxidizing conditions. (a) Experimental design of accelerated degradation and swelling studies. (b) Swelling ratio of PHT polymers under aqueous (HBSS), alkaline (5 N NaOH) and acidic (1 N HCl) conditions after 4 h at room temperature (n = 6 for each group; 1 independent experiment). (c) Accelerated degradation of PHT polymers under alkaline (5 N sodium hydroxide/NaOH), acidic (2 N hydrochloric acid/HCl), and oxidizing (30% hydrogen peroxide/H_2O_2) conditions at room temperature over 5 days or 1 week (5 N NaOH – PHT polymer: n = 28, ADM: n = 9, 2 N HCl – PHT polymer: n = 14, ADM: n = 9, 30% H_2O_2 – PHT polymer: n = 6, ADM: n = 3; 1–2 independent experiments). ****: $p \leq 0.0001$; statistical significance was relative to ADM. (d) Percentage change in tensile strength, tensile modulus, and failure strain following 1-week incubation in 2 N HCl (PHT polymer: n = 14, ADM: n = 6; 1 independent experiment). Error bars indicate standard error of mean.

further supported 3D-printed PHT scaffold cytocompatibility, with hMSCs adopting an elongated and well-spread morphology on the surface of the PHT scaffold (Fig. 5d). Together, these results demonstrated that PHT polymer was cytocompatible.

2.5.2. *Tenogenic differentiation assay on PHT polymer*

To further assess the ability of PHT polymer to support tendon-like differentiation, hMSCs were cultured on the surface of PHT polymers in the presence or absence of tendon-promoting FGF-2 and TGF-β3 for 4 days or 10 days followed by Picrosirius Red staining for collagen and immunostaining for tendon-associated markers including scleraxis (Scx), collagen type I (Col1), tenascin C (Tnc) and tenomodulin (Tnmd) (Fig. 5a). Increased Picrosirius Red staining was observed for hMSCs cultured on PHT polymers with FGF-2 and TGF-β3 (2h-$PHT_{FGF\text{-}2+TGF\text{-}\beta3}$: 0.50 ng/mL Col1, 4h-$PHT_{FGF\text{-}2+TGF\text{-}\beta3}$: 0.58 ng/mL Col1, 8h-$PHT_{FGF\text{-}2+TGF\text{-}\beta3}$: 0.44 ng/mL Col1) relative to untreated controls (2h-$PHT_{Control}$: 0.28 ng/mL Col1, 4h-$PHT_{Control}$: 0.36 ng/mL Col1, 8h-$PHT_{Control}$: 0.18 ng/mL Col1), indicating increased collagen deposition (Fig. 5e). Immunofluorescence staining also revealed that hMSCs cultured on the surface of PHT polymers with FGF-2 and TGF-β3 showed a 2.6-, 520-, 3.6-, and 29.7-fold increased expression for Scx (day 4), Col1 (day 10), Tnc (day 10), and Tnmd (day 10) relative to control (Fig. 5f). Together, these data demonstrated that PHT polymer supported hMSCs tendon-like differentiation.

2.6. *In vivo characterization of 3D-printed PHT scaffold*

2.6.1. *Mouse dorsal subcutaneous implantation and histology*

To assess the *in vivo* biocompatibility of PHT polymer, ADM and 3D-printed PHT scaffolds fabricated from 4h-PHT were implanted subcutaneously in mice for 3 weeks and assessed histologically (Fig. 6). Mice implanted with either ADM or 3D-printed PHT scaffolds showed consistent weight gain and did not exhibit adverse clinical signs or mortality (**data not shown**) or detrimental reactions such as necrosis, infection, and granuloma around the implants as assessed by gross visual inspection (Fig. 6a). Hematoxylin and Eosin (H&E) staining showed that

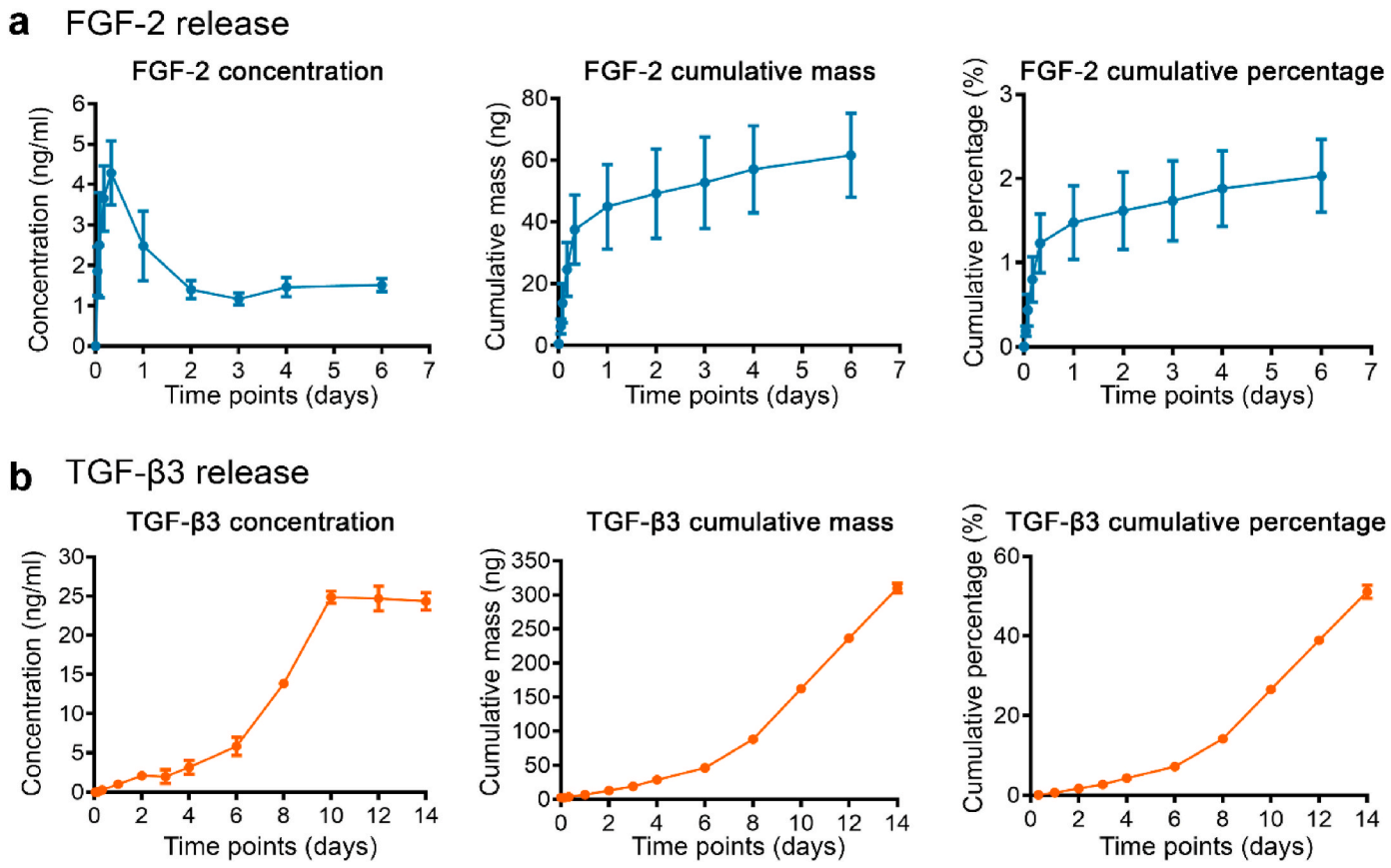

Fig. 4. Growth factor release profile from 3D-printed PHT scaffold. 3D-printed PHT scaffolds containing fibrin gels mediated controlled release of FGF-2 and TGF-β3. (a) Concentration, cumulative mass and cumulative percentage of FGF-2 released from the fibrin gel inside the PHT scaffold. (b) Concentration, cumulative mass and cumulative percentage of TGF-β3 released from the fibrin gel inside the PHT scaffold. Experiments were repeated twice with n = 2 independent experiments for each time point.

3D-printed PHT scaffold did not induce an overt inflammatory response as ADM (Fig. 6b). In support of this, negligible staining for inducible nitric oxide synthase (iNOS) and CD68 monocyte/macrophage marker was observed in tissues adjacent to both 3D-printed PHT scaffold and ADM (Fig. 6b). Although some positive iNOS and CD68 staining signals were observed, these largely originated from skeletal muscle fibers or non-specific staining of 3D-printed PHT and ADM as opposed to monocytes/macrophages (Fig. 6b). Together, these findings demonstrated that 3D-printed PHT scaffold was biocompatible.

2.6.2. Rabbit large-to-massive rotator cuff injury, tensile testing, and histology

To assess the ability of bioactive PHT polymer to treat severe tendon injuries, 3D-printed PHT scaffolds were fabricated from 4h-PHT, combined with fibrin hydrogel containing either no growth factor or with FGF-2 and TGF-β3 just prior to surgery, and implanted into a rabbit large-to-massive rotator cuff injury (0.3-cm segmental defect with 1-cm gap) for 8-weeks followed by biomechanical and histological assessment (Fig. 7). This study did not perform ADM-mediated repair since PHT polymer exhibited superior native tendon-like tensile properties and higher physical integrity relative to ADM and repair interventions were compared to contralateral intact/uninjured control as a gold standard. Also, this study protocol used a 1-cm gap to both simulate a large-to-massive injury with tendon retraction (Fig. 7a–b) as well as to reduce excessive repair tension, the latter of which has been shown to be detrimental to long-term repair integrity [46]. Rabbits implanted with 3D-printed PHT scaffolds showed consistent weight gain and did not exhibit unrelated adverse clinical signs or mortality (**data not shown**).

Mechanical testing of the supraspinatus muscle-tendon-bone units 8-weeks post-surgery (Fig. 7c–h) demonstrated that rabbits implanted with 3D-printed PHT scaffolds exhibited excellent restoration of shoulder mechanical properties. Specifically, PHT-GFs (PHT with FGF-2 and TGF-β3) showed higher ultimate load (Control: 55.33 ± 2.82 N; PHT: 69.16 ± 6.22 N; PHT-GFs: 79.49 ± 3.96 N) and similar stiffness (Control: 13.30 ± 0.80 N/mm; PHT: 10.43 ± 1.13 N/mm; PHT-GFs: 10.44 ± 1.18 N/mm) when compared to the no surgery/uninjured control group (Fig. 7d and e). The ultimate displacement in both PHT and PHT-GFs groups were also higher (Control: 6.21 ± 0.44 mm; PHT: 12.69 ± 1.17 mm; PHT-GFs: 11.01 ± 1.29 mm) compared to no surgery/uninjured control group (Fig. 7f). This higher ultimate displacement resulted in a 2- to 3-fold increased total work-to-failure (Control: 0.22 ± 0.02 J; PHT: 0.59 ± 0.06 J; PHT-GFs: 0.54 ± 0.09 J), which endowed an additional factor of safety to avoid catastrophic failure of the repair construct (Fig. 7g). Similar results were attained with higher FGF-2 and TGF-β3 doses (**data not shown**). Notably, PHT scaffold with or without FGF-2 and TGF-β3 showed the highest normalized ultimate load and normalized stiffness when compared to recent tendon tissue engineering studies that reported both tensile strength and modulus along with uninjured limb as control (Fig. 7h and Table S2-**S3**), highlighting 3D-printed PHT scaffold's favourable mechanical properties [47–50].

Histological assessment of the supraspinatus muscle-tendon-bone units 8-weeks post-surgery demonstrated the presence of at least 1-cm of regenerated tendon tissue in 67% of rabbits (n = 4/6) in PHT group and 100% of rabbits in PHT-GFs group (n = 6/6) as shown in the H&E, Masson's Trichrome, and Picrosirius Red stains (Fig. 7i). Elongated cells with flattened nuclei embedded within aligned and wavy collagen fibers were observed in all 3D-printed PHT scaffold groups as shown in the H&E staining, and Picrosirius Red staining showed increased collagen

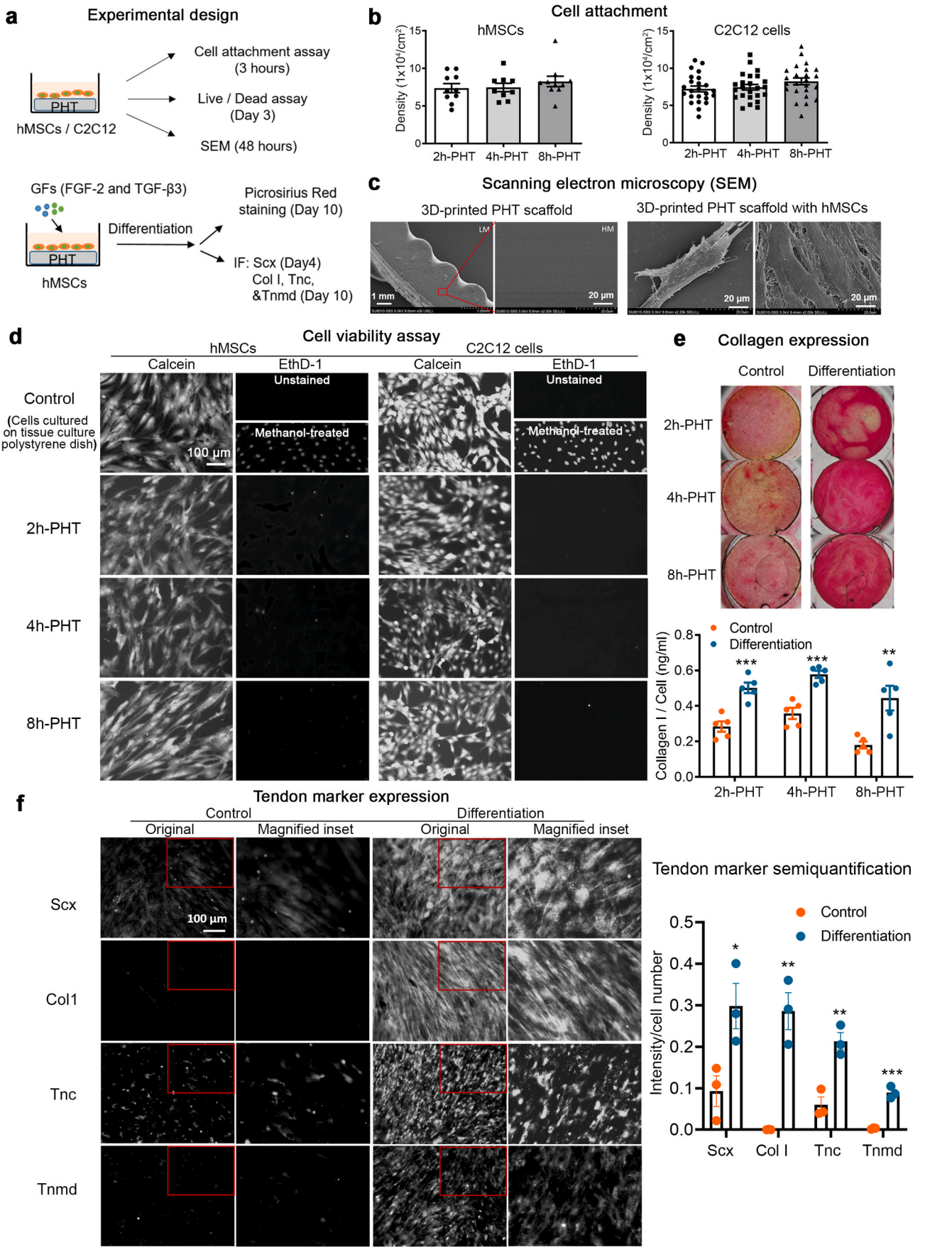

(caption on next page)

Fig. 5. Effect of PHT polymers on hMSC and C2C12 cell attachment, hMSC and C2C12 cell viability and hMSC tendon-like differentiation *in vitro*. PHT polymers exhibited cytocompatibility with hMSCs and C2C12 cells and supported growth factor-mediated tenogenic differentiation. (a) Experimental design. (b) Cell attachment assay. hMSCs and C2C12 cells exhibited similar attachment number on the surface of PHT polymer post-heat cured for 2, 4 and 8 h (hMSCs: n = 10, C2C12 cells: n = 24, 2 independent experiments). (c) SEM images of 3D-printed PHT scaffold with and without hMSCs. (d) Cell viability assay. hMSCs and C2C12 cells maintained high viability on PHT polymers after 3 days culture (n = 2 for each group, 2 independent experiments). Viable cells (Calcein) stained the cytoplasm whereas dead cells (EthD-1; ethidium bromide) stained the nucleus. (e) Picrosirius Red staining of control and differentiated hMSCs cultured on the surface of PHT polymer post-heat cured for 2, 4 and 8 h separately. Collagen expression level was normalized with cell densities (n = 5 for each group, 2 independent experiments). *: $p \leq 0.05$; **: $p \leq 0.01$; ***: $p \leq 0.001$, statistical significance was relative to control group. (f) Representative immunofluorescence images of Scx, Col1, Tnc and Tnmd expression on hMSCs after 4- (Scx) and 10-days (Col1, Tnc and Tnmd) culture on PHT polymer with 4 h post-heat curing in control and differentiation medium. Expression level was normalized to cell density (n = 3 for each group, 2 independent experiments). Error bars indicate standard error of mean. *: $p \leq 0.05$; **: $p \leq 0.01$; ***: $p \leq 0.001$, statistical significance was established relative to the control group.

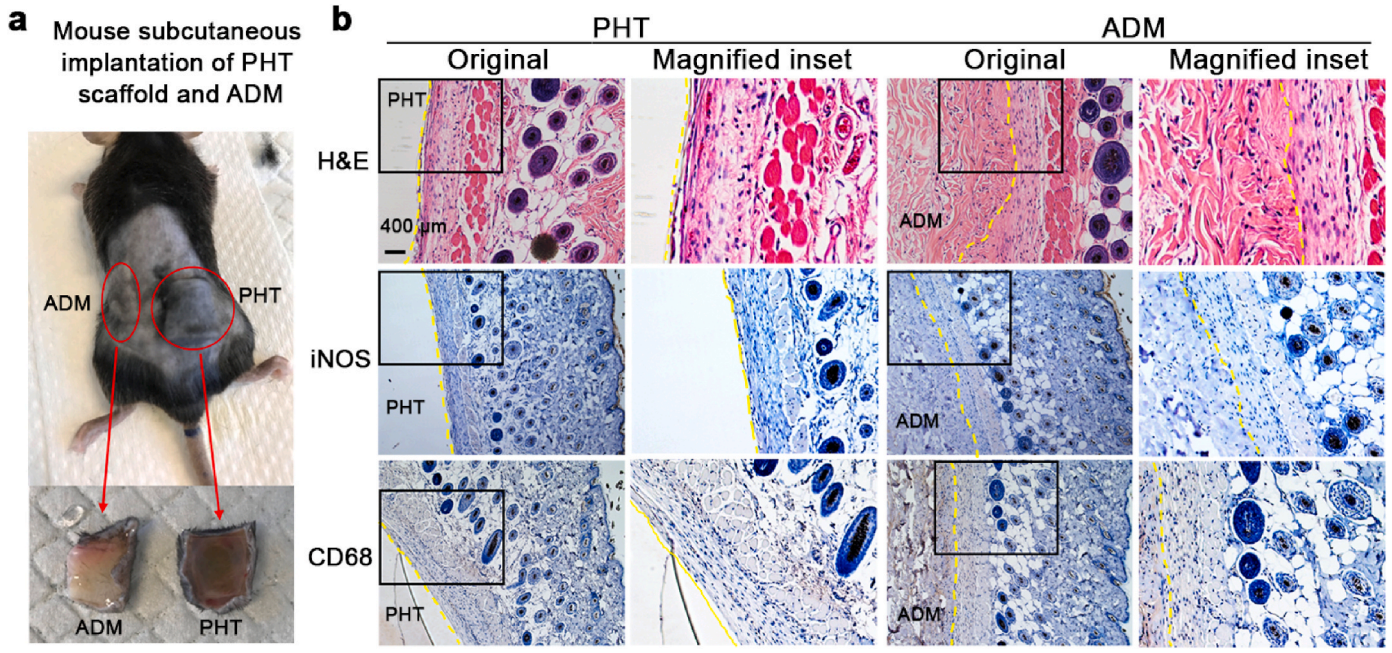

Fig. 6. *In vivo* characterization of 3D-printed PHT scaffold in mouse dorsal subcutaneous implantation model. 3D-printed PHT scaffold and ADM exhibited biocompatibility. (a) Representative photos of mouse dorsal subcutaneous implantation of 3D-printed PHT scaffold and ADM and samples collected 3-weeks post-surgery. (b) Representative H&E images and immunohistochemistry staining images of inducible nitric oxide synthase (iNOS) and CD68 inflammation-associated markers. Yellow dotted lines indicate the border between 3D-printed PHT scaffold or ADM with adjacent mouse skin tissue. Sample number n = 3 for each group. Scale bars as indicated in the images.

content in the region of interest (ROI) for the PHT-GFs group relative to the PHT group (Fig. 7i), whereas the two groups showed similar level of collagen alignment in the ROI (Fig. S4). Blinded histological scoring showed that the PHT-GFs group exhibited a favourable lower macroscopic histopathological score (closer to no surgery/uninjured group) than the PHT group indicating the application of FGF-2 and TGF- β3 improved the regeneration of tendon tissue 8 weeks after surgery (Fig. 7j and Table S4). However, the microscopic histopathological scores between the two groups were similar (Fig. S4 and Table S5). In addition, immunofluorescence staining of tendon-associated markers showed positive staining for Scx, Col1 and Tnmd peri-implant in all 3D-printed PHT scaffold groups, with higher Scx expression in the PHT-GFs group (Fig. 7k).

Together, these data demonstrated that 3D-printed PHT scaffold with FGF-2 and TGF-β3 fully restored SST rotator cuff tensile properties and promoted at least 1-cm of tendon regeneration.

3. Discussion

3.1. Goal of this work

The primary motivation in this work was to develop an easily manufactured, mechanically robust, and pro-regenerative tendon biomaterial that addresses mechanical and biological deficits in rotator cuff injuries whilst avoiding a complex and laborious production process. From a manufacturing perspective, PHT pre-polymer resin could be rapidly prepared in under 30 min at ambient room temperature conditions for 3D-printing (Fig. 1). From a mechanical repair perspective, 3D-printed PHT polymer was mechanically strong and tendon-like (Fig. 2), exhibiting slow degradation to facilitate physiological shoulder movement and preserve surgical repair integrity (Fig. 3). From a biological repair perspective, 3D-printed PHT polymer was amenable to controlled growth factor delivery (Fig. 4), supported growth factor-mediated tenocyte differentiation *in vitro* (Fig. 5), and exhibited similar biocompatibility as tendon clinical grafts in an ectopic mouse subcutaneous model (Fig. 6), which are crucial requirements for enhancing tissue healing. Notably, 3D-printed PHT polymer with growth factors demonstrated at least 1-cm of tendon regeneration with native-like biomechanical attributes as uninjured shoulder in an orthotopic rabbit rotator cuff injury model (Fig. 7). Together, this study shows that 3D-printed PHT polymer has potential for rapid and seamless manufacture of patient personalized grafts whilst simultaneously addressing mechanical and biological deficits in rotator cuff injuries.

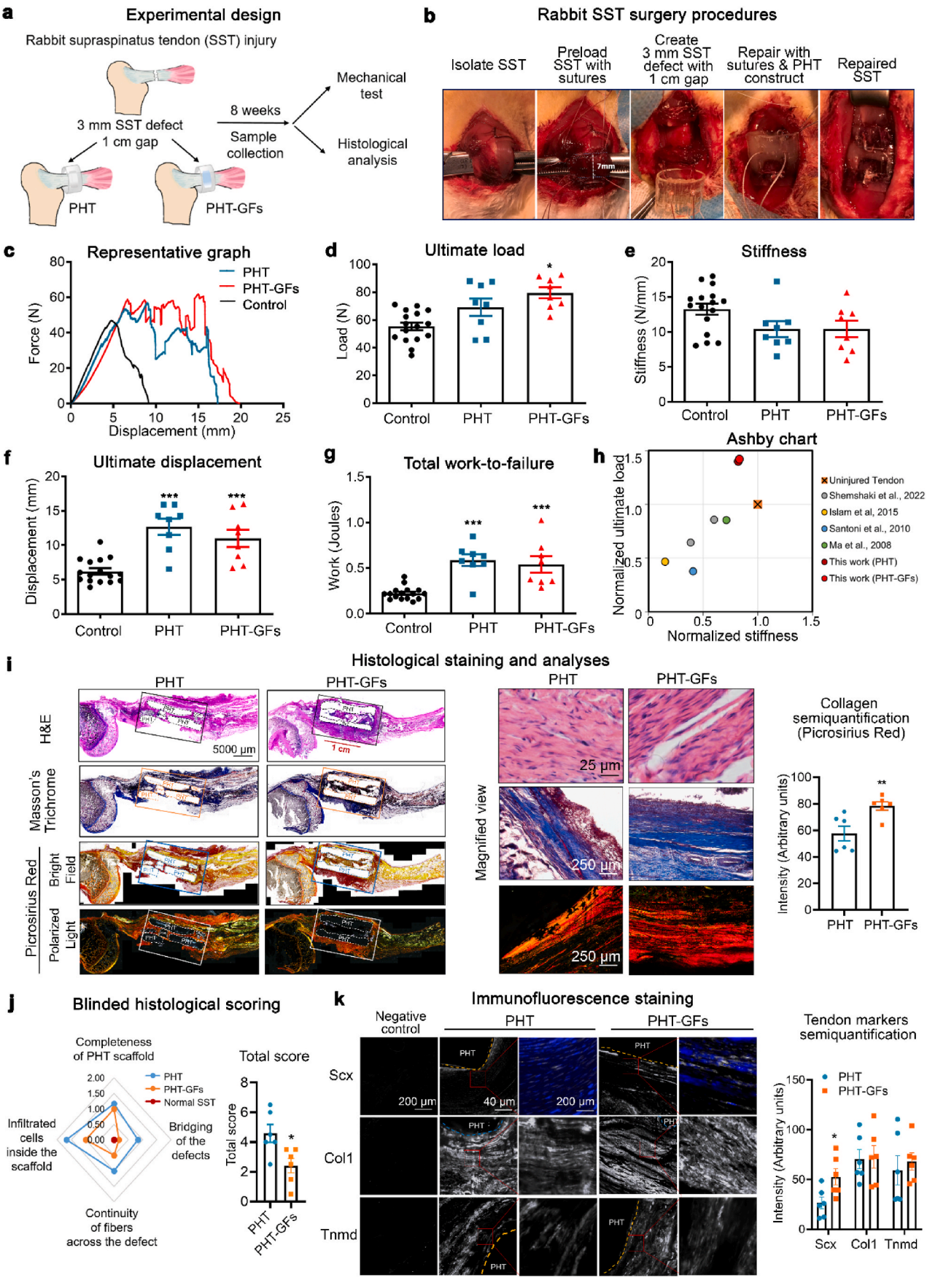

(caption on next page)

Fig. 7. Biomechanical properties and histological assessment of the rabbit humeral bone-SST tissue samples 8-weeks post-surgery. 3D-printed PHT scaffolds containing FGF-2 and TGF-β3 (PHT-GFs) facilitated at least 1-cm of tendon regeneration and exhibited native supraspinatus tendon (SST)-like mechanical properties. (a) Experimental design for *in vivo* characterization of 3D-printed PHT scaffold in rabbit SST injury model. (b) Rabbit SST surgery procedures. (c) Representative force-displacement curve. (d) Ultimate load was increased in PHT-GFs group compared to the intact control group. (e) Stiffness was similar between PHT and PHT-GFs compared to the intact control group. (f) Ultimate displacement was increased in PHT and PHT-GFs compared to the intact control group. (g) Total work-to-failure was increased in PHT and PHT-GFs compared to the intact control group. (h) Ashby chart simultaneously comparing ultimate load and stiffness of repaired tendon constructs normalized to their uninjured tendon control showed that this work (PHT and PHT-GFs) attained the highest normalized ultimate load and stiffness. Panels (d), (e), (f), and (g) – Control: n = 16, PHT: n = 8, PHT-GFs: n = 8. *: Statistical significance ($p \leq 0.05$), **: $p \leq 0.01$; ***: $p \leq 0.001$ relative to intact control group. (i) Representative H&E, Masson's Trichrome and Picrosirius Red (brightfield and under polarized light microscopy) staining of PHT and PHT-GFs samples. Longitudinal sections showing humeral bone and SST were used. Black, orange and blue rectangles represent the region-of-interest (ROI) used for semiquantification (left). Dotted lines demarcate regions of 3D-printed PHT scaffold and are labeled with 'PHT'. Scale bar = 5000 μm. Representative high magnification images of H&E, Masson's Trichrome and Picrosirius red staining (polarized light images) showing the regenerated tendon fibers in PHT and PHT-GFs group (right). Collagen expression was semi-quantified by the signal intensity in the ROI of Picrosirius Red-stained brightfield images. (j) Macroscopic histopathological score. Radar charts showed that PHT-GFs attained macroscopic histopathological scores similar to normal SST relative to PHT group. (k) Representative images of immunofluorescence staining for tendon-associated markers Scx, Col1 and Tnmd with no primary antibody control. Orange dotted lines indicate the border between PHT scaffold and adjacent tissues. Red lines indicate the enlarged region. Semiquantification of tendon markers expression. Scale bars as indicated in the images. Panels (i) and (j) – Sample number n = 6 for each group. *: Statistical significance ($p \leq 0.05$); **: $p \leq 0.01$.

3.2. Prior advances in tendon biomaterial scaffolds

In recent years, numerous tissue engineering studies have made significant technical and conceptual advancements and contributions to tackle the development and fabrication of mechanically competent and pro-regenerative tendon biomaterial scaffolds for clinical repair. These include novel strategies based on cells [51–58], biological/biochemical cues [51,59–66], and biomaterial scaffolds [25,30,40,51,54,55,67–73] as well as commercially available collagenous matrices such as GraftJacket™, Restore Orthobiologic Implant™ and Zimmer® Collagen Repair Patch [30] or commercially available synthetic polymers such as polyurethane-based SportsMesh Soft Tissue Reinforcement/Artelon® [30]. This body of work has made significant progress in the development of next-generation tendon therapeutics. For example, anisotropic composite hydrogels comprised of stiff aramid nanofibers and soft polyvinyl alcohol achieved high tendon-like tensile strength and modulus of 72 MPa and 1.1 GPa, respectively [33], while growth factors such as GDF-5, GDF-6, and GDF-7 have been shown to induce ectopic tendon *in vivo* [64]. However, it is worth noting that several advancements in this field involve time-consuming and labor-intensive fabrication processes. These may include, for example, prolonged high temperature stirring for several days to attain dispersion solutions that produce scaffolds with robust tendon-like mechanical properties. Additionally, complex combinations of cells, multi-material scaffolds, and biological/biochemical cues are often employed to stimulate pro-tendon regenerative activity. Unfortunately, these intricate fabrication methods can escalate production costs and impede swift clinical implementation. Overall, there is a scarcity of facile and rapid fabrication techniques that can produce pro-regenerative biomaterial scaffolds with mechanical characteristics similar to native tendon tissue for treating large-to-massive rotator cuff injuries.

3.3. 3D-printed PHT scaffold addresses facile manufacturability

Considering that typical synthesis of polyurethane-based elastomers takes place at elevated temperatures for extended durations [74], the ability to prepare visible light-crosslinkable resins in as little as 30 min via simple mixing under ambient room temperature conditions is highly attractive in terms of enabling on-demand, on-site manufacturing and increased occupational safety.

From a facile manufacturing perspective, the rapidity of this reaction in the absence of heating under an inert atmosphere is due to the fast and oxygen-permissive nature of thiol-isocyanate and thiol-acrylate reactions, which results in the formation of a polythiourethane acrylate network (Fig. 1, **S1**, and **S2**) [75–79]. Concurrent with these thiol-Michael addition click reactions, acrylate-acrylate homopolymerization reactions are likely to occur and have been reported in similar polymerization systems [75–78]. Furthermore, as an on-site, additive manufacturing technology, 3D-printing can eliminate costly logistical transportation, reduce material wastage for low-volume, on-demand production, 3D-fabricate complex scaffold geometries personalized for a patient's specific shoulder anatomy and rotator cuff lesion (i.e., tear size and shape) [22,23], and control porosity for cell colonization and incorporation of tendon-promoting growth factors and drugs [80,81]. Indeed, prior studies have elucidated how different tendon tear shapes generate different strain profiles during shoulder movement [22]. As such, 3D-printed tendon graft can be customized for particular tear morphologies to reduce stress via *in silico* methods such as finite element analysis [82] and minimize the likelihood of re-tears. As such, a photocrosslinkable resin that can be easily prepared within a relatively short duration would aid on-site and on-demand production of 3D-printed tendon grafts with the potential to address patient-specific tear morphologies.

From an occupational safety perspective, reduced exposure to harmful substances or radiation during biomaterial fabrication is highly desired. In the industrial manufacture of polyurethane polymers, two-step chemical reactions involving excess isocyanate stoichiometry are typically employed to achieve robust control of chemical reactivity [74]. However, such an approach may pose health hazards to workers via accidental skin contact with highly toxic isocyanates [83]. Our approach is distinct from current convention in that PHT pre-polymer resin is prepared with excess thiol stoichiometry, which similarly allows for robust control of chemical reactivity while ensuring that isocyanates are mostly or fully reacted prior to 3D-printing (Fig. 1). This same approach can be applied using other multi-functional thiols (-SH) and polyols (-OH) to generate a versatile library of photo-crosslinkable polyurethanes with desired material attributes. Furthermore, the ability to 3D-print PHT polymer using abundant and relatively innocuous visible light overcomes disadvantages typically associated with high-energy UV systems such as increased cost and occupational harm [79,84]. As such, a visible light-crosslinkable resin employing excess thiol stoichiometry can achieve robust control of chemical reactivity whilst reducing exposure to hazardous UV radiation and toxic isocyanates.

3.4. 3D-printed PHT scaffold can address mechanical deficits

To facilitate shoulder recovery, rotator cuff scaffolds must exhibit clinical characteristics conducive for maintaining the integrity of a surgically repaired tendon as well as native tendon-like mechanical properties for facilitating joint movement.

From a repair integrity perspective, important clinical attributes a biomaterial scaffold should possess include high suture retention, high total-work-to-failure, and slow degradation. The former two characteristics are indicative of a graft's ability to resist suture pullout/tearing and the amount of energy a graft can sustain before physical failure while the latter preserves graft integrity over the long durations required

for tissue healing to complete. In this respect, the ability of 4h-heat cured, 3D-printed PHT scaffold to resist suture tearing (8.62-fold lower suture migration) and absorb 2-fold higher energy before physical failure relative to clinically available ADM underscores the mechanical resilience of 3D-printed PHT scaffold in ensuring surgical repair integrity (Fig. 2). Given that the wound microenvironments fluctuate between acidic and alkaline conditions during different stages of healing with chronic wounds typically showing increased alkalinity (e.g., pH 7.2–8.9) [85–88] and foreign body reactions comprising of oxidative environments [25], the slower degradation of PHT polymers indicate prolonged maintenance of physical integrity including tensile properties relative to ADM (Fig. 3). The slower degradation under alkaline conditions is notable given that a significant portion of rotator cuff tears are chronic in nature [1–3]. Such prolonged graft integrity is expected to better support surgical repair owing to longer maintenance of tensile strength and additional time to facilitate host cell in-growth and healing following implantation [88]. Indeed, porcine-based collagen matrices that degrade too rapidly have been reported to fail within 3–6 months post-treatment [89]. For this reason, numerous implant materials used in rotator cuff repair such as sutures (e.g., Arthrex FibreWire®) and suture anchors (e.g., Corkscrew®) are made of slowly degrading or non-degradable biomaterials such as ultra-high molecular weight polyethylene and polyether ether ketone/PEEK. As such, 3D-printed PHT scaffolds exhibit excellent resistance against suture tearing and durable scaffold integrity for maintaining the long-term integrity of a surgically repaired rotator cuff construct.

From a physiological loading perspective, mechanical properties including native tendon-like tensile attributes and robustness to both static as well as cyclic tensile forces are necessary for enabling/restoring shoulder movement. Given that tendon midsubstance was identified as the predominant location for muscle-tendon-bone injuries [4], this study specifically aimed to address large-to-massive tendon-only tears. This work does not belie the significance of bone-tendon repair or that rotator cuff tissues are mechanically inhomogeneous [70]. Although not explored in this study, these concerns can be addressed by combinatorial use of finite element analysis with biomaterials that possess photo-tunable mechanical properties for a geometrically- and mechanically-optimized graft [25,70,82]. In this respect, the tensile strength (23.3 ± 0.50 MPa) and tensile modulus (459.4 ± 17.13 MPa) of 4h-PHT were well-matched with those of human SST (tensile strength: 4–22 MPa, tensile modulus: 218–592 MPa [11,12]), while 8h-PHT's tensile modulus (843.7 ± 31.97 MPa) was well-matched with those of human Achilles tendon (tensile modulus: 816 ± 218 MPa) [90]. Although clinically available tendon grafts may have similar tensile strength as PHT polymer (11.9–32.7 MPa), they possess markedly lower tensile moduli (14–71 MPa) [30], which is expected to impede the efficiency of musculoskeletal movement [13]. As evidence of robustness to static and cyclic tensile forces, 2h-, 4h-, and 8h-PHT polymers sustained at least 10,000 cycles of tensile loading at levels comparable to 75% of the failure stress observed for human SST (as reported by Itoi et al.) [11,25] with stable dynamic, storage and loss moduli, whilst 4h- and 8h-PHT exhibited 3.67- to 4.10-fold faster creep recovery relative to clinically available ADM (Fig. 2). These robust tensile properties enabled 3D-printed PHT scaffold to biomechanically restore injured supraspinatus rotator cuff units to levels comparable with uninjured contralateral limbs following 8-weeks implantation in a large-to-massive (1-cm gap) rabbit SST injury model (Fig. 7). As such, 3D-printed PHT scaffolds exhibit robust tendon-like tensile properties *ex vivo* and *in vivo* to restore shoulder biomechanical functionality.

3.5. 3D-printed PHT scaffold with growth factors can address biological deficits

To enhance tissue healing, rotator cuff biomaterial scaffolds must avoid a strong immune response that would ultimately lead to graft rejection whilst possessing the ability to control the release of bioactive factors for inducing robust tendon-like differentiation.

From a biocompatibility perspective, 3D-printed PHT scaffold exhibited similar immune response as clinically available ADM in terms of gross morphology as well as iNOS and CD68 staining following three-week subcutaneous implantation in mice (Fig. 6). Although overt inflammation was not observed for 3D-printed PHT scaffolds and clinically available ADM, Tu et al. and others have posited that engineering biomaterials with the ability to control inflammation offers a novel strategy for enhancing therapeutic effect [91–96]. For example, matrix metalloproteases (MMPs) are extracellular matrix remodelling enzymes found in high abundance during inflammation and can regulate immune cell responses during disease [95] or injury [93]. Taking advantage of this knowledge, Cai et al. developed an MMP-2 responsive hydrogel-electrospun patch that delivers TGF-β1 siRNA to reduce undesired fibroblast proliferation and peritendinous adhesions [91] while Zhang et al. similarly developed MMP-responsive polyethylene glycol-based hydrogels that release phosphatidylserine to accelerate macrophage transition towards an anti-inflammatory M2 phenotype for improved bone regeneration [96]. Given that 3D-printed PHT scaffold can be combined with hydrogels for controlled bioactive factor delivery, a similar strategy incorporating use of immunomodulatory factors can be implemented in future work. As such, 3D-printed PHT scaffold is biocompatible.

From a drug delivery perspective, the combination of 3D-printed PHT polymer with fibrin extracellular matrix endowed our tissue engineered scaffold with the ability to retain and release bioactive factors such as FGF-2 and TGF-βs in a controlled manner (Fig. 4). These growth factors are known to exhibit a natural affinity for extracellular matrix molecules such as fibrinogen and bind to them in a non-covalent manner [36,37]. Such affinity-based binding has been successfully utilized for immobilizing growth factors *in situ* for spatial control of cell differentiation [38–40,71]. This versatile approach also allows for drugs, growth factors, and other biochemical cues to be combined with 3D-printed PHT scaffold at the time of surgery, which can preserve bioactivity for maximal therapeutic effect (Fig. 7). Alternatively, other methods of controlled bioactive factor delivery may be considered for use with 3D-printed PHT scaffolds. For example, metal-phenolic-based materials such as nanofillers, nanosponges, and nanocloaks have been reported [97–100]. These metal-phenolic-based materials can undergo self-assembly into hierarchical supramolecular structures and when embedded within hydrogels, exhibit targeted and controlled drug release in response to specific environmental triggers [97–100]. In agreement with prior tissue engineering studies [1,29,38–40,62,63], FGF-2 and TGF-β3 were tenogenic and promoted tendon-like differentiation of human mesenchymal stem cells *in vitro* (Fig. 5) and *in vivo* (Fig. 7). Notably, 3D-printed PHT scaffold with growth factors showed at least 1-cm of neotendon regeneration across the injury gap in a large-to-massive rabbit rotator cuff injury model, demonstrating a strong and robust healing response, which included increased collagen content and a histological score that was more similar to native SST relative to no growth factor control (Fig. 7). As such, 3D-printed PHT scaffold can be used for controlled delivery of growth factors to biologically augment tendon-like regeneration *in vitro* and *in vivo* for accelerating the slow and oft-incomplete tendon healing process.

4. Conclusion

In summary, we have developed a rapid and facile approach that produces 3D-printable resins in about 30 min under ambient, room temperature conditions. With this technique, mechanically robust slow degrading polythiourethane elastomer known as PHT polymer was 3D-fabricated and used to deliver bioactive FGF-2 and TGF-β3 for large-to-massive tendon repair. Notably, 3D-printed PHT polymer/scaffold was (i) mechanically robust with human supraspinatus tendon-like tensile attributes and withstood 10,000 cycles of physiologic tensile loading without failure and (ii) delivery of FGF-2 and TGF-β3 fully restored

tendon biomechanical function to native, uninjured levels and regenerated 1-cm of rotator cuff tendon tissue. Altogether, the technical advances developed here demonstrate rapid and facile production of 3D-printable pre-polymer resins, with PHT polymer holding significant potential for treatment of large-to-massive rotator cuff repair as well as other soft tissue injuries.

5. Materials and methods

5.1. Synthesis and ex vivo chemical characterization of PHT polymer and 3D-printed PHT scaffold

5.1.1. Synthesis of PHT polymer

The fabrication of PHT polymer involved a two-step reaction. Pentaerythritol tetra (3-mercaptopropionate) (P; Sigma Aldrich, USA, #381462), hexamethylene diisocyanate (1,6-Diisocyanatohexane) (H; TCI Chemicals, USA, TCI-H0324), trimethylolpropane triacrylate (stabilized with MEHQ) (T; Sigma Aldrich, USA, #246808), N,N,N′,N′-tetrakis(2-hydroxy-propyl) ethylenediamine (quadrol or Q; Sigma Aldrich, USA, # 122262), 1,2-dicyclohexyl-4,4,5,5-tetramethylbiguanidium n-butyltriphenylborate (FUJIFILM Wako Pure Chemical Co., Japan, WPBG-300), 2-isopropylthioxanthone (FUJIFILM Wako Pure Chemical Co., Japan, IPTX) and acetone (RCI Labscan, Thailand, #AR1003) were used as received without purification. In the first step, P was first mixed with 10 μL Q solution (33.3% v/v, in acetone) as catalyst in a 50 mL conical tube and vortex for 30 s for mixing. Subsequently, H was added to the mixture at a molar ratio of 5:1 (-SH: NCO) of the functional group, and vortex at 2500 revolutions per minute (rpm) at room temperature (RT) for 20–30 min to allow complete reaction of H and generate a PH pre-polymer. In the second step, T was added to form a mixture that contained achieve a functional group ratio of 5:1:6 for thiol:isocyanate: acrylate for subsequent photocrosslinking. To facilitate photocrosslinking, acetone (10 % of total volume) was added to the PHT mixture for reducing viscosity whereas WPBG-300 photocrosslinker solution (10% w/v, in acetone) and IPTX photosensitizer solution (10% w/v, in acetone) were added in a 5:1 WPBG-300:IPTX volumetric ratio to facilitate photocrosslinking under ambient conditions with visible light. This final mixture was ready for 3D printing and referred to as PHT resin.

This study employed 3D-printed samples and mechanical testing samples, which were fabricated using a Kudo Titan 2 HR 3D printer (Kudo3D, https://www.kudo3d.com/) according to the manufacturer's instructions. For synthesizing 3D-printed samples, the desired 3D model was sliced at a thickness layer of 0.5 mm using Creation Workshop software (Envision Labs, USA) and uploaded into the 3D printer. Subsequently, PHT resin was transferred into a resin container and each layer received visible light (405 nm) exposure for 150 s. For synthesizing mechanical testing samples, the PHT resin was transferred into a modified Type V mold (ASTM D638-10) and photocrosslinked using the Kudo Titan 2 HR 3D printer as a light source for 150 s. Subsequently, photocured PHT polymer samples were heat cured in a vacuum oven (SVAC1-2 Compact Vacuum Drying Oven, Shel Lab, USA) at 150 °C for 2, 4, or 8 h separately to produce 2h-PHT, 4h-PHT, and 8h-PHT, respectively. Samples were washed with 5 N NaOH (Thermofisher, USA) for 1 h and 1 × phosphate buffered saline (PBS; Thermofisher, USA) buffer three times. Before *in vitro* and *in vivo* use, samples were sterilized under UV light for 30 min in a cell culture hood (Thermofisher, USA).

5.1.2. 3D computer aided design (CAD) modelling of PHT scaffold

CAD of PHT scaffold was performed using Micorosoft 3D Builder software (Microsoft Corporation, USA). The scaffold was designed as a sheath-like structure with dimensions of 14 × 6.5 × 14 mm (length × width × height) and thickness of 0.8 mm. Five connected strips of hemicylindrical shape with a radius of 0.5 mm were designed at the two inner sides to act as topographical cues for cells. Four hemispherical shapes were added on each side to serve as landmarks for suturing. 3D CAD models were processed for 3D-printing as described in 'Synthesis of PHT polymer'.

5.1.3. Fourier transformed infrared (FTIR) spectroscopy

FTIR was performed by Nicolet Is10 FT-IR spectrometer (Thermofisher, USA) according to the manufacturer's instructions. PHT pre-polymer samples were prepared at a functional group ratio of 5:1:6 for thiol:isocyanate:acrylate. P, H, T and PHT pre-polymer samples were placed between two salt plates, which were subsequently mounted onto the sample holder. The chamber was filled with inert nitrogen gas for 1 min before acquiring spectra. All spectra were recorded (7800–350 cm^{-1} spectra range) at a resolution of better than 0.4 cm^{-1}. Spectra were baseline-corrected and analyzed in OMNIC™ Series Software (Thermofisher, USA).

For studies of PHT polymer samples under conditions of increased photocrosslinking, thin polymer films were generated. These thin films were created by placing PHT pre-polymer on the top of a small piece of parafilm, which was subsequently sandwiched between two glass slides, and photo-crosslinked using the Kudo Titan 2 HR 3D printer as a light source for 10, 20, 30, or 60 s. Samples were similarly placed between two salt plates and mounted onto the sample holder. Spectra were recorded (350–7800 cm^{-1} spectra range) at a resolution of better than 0.4 cm^{-1}. Spectra were baseline-corrected and analyzed in OMNIC™ Series Software (Thermofisher, USA). For analysis of photocrosslinking-induced changes, the area under peaks-of-interest were computed, normalized to the peak at 780 ± 5 cm^{-1} (attributed to the bending mode of –CH), and data were fitted using a polynomial (order 2) model.

5.1.4. MicroCT imaging

The microCT image reconstruction of the 3D-printed PHT scaffold was performed with Scanco Medical μCT 35 (SCANCO Medical AG, Switzerland). The PHT scaffold was placed in a holder (Φ 20 mm × H 75 mm) and scanned with the following X-ray settings (Energy/Intensity: 45 kVp, 88 μA, 4 W; Integration time: 300 ms) at medium resolution. The 3D images were reconstructed using the Scanco Medical μCT 35 software (SCANCO Medical AG, Switzerland).

5.2. Ex vivo mechanical characterization of PHT polymer and 3D-printed PHT scaffold

PHT samples were mechanically tested using either a Tinius Olsen H25KS tensile testing machine (MTX0280-Model-H25KS, Tinius Olsen, USA) equipped with a 250 N load cell or an ADMET mechanical tester (ADMET, USA) equipped with a 100 lb (445 N) load cell, with data analyzed using Microsoft Excel (Microsoft Corporation, USA). Static tensile, cyclic tensile, static creep tensile test samples were fabricated similar to the guidelines in the American Society for Testing and Materials methods (ASTM-D638-10). These samples were fabricated as type V dog bone-shaped specimens with an overall length of 36.12 mm and the narrow region of 1.82 mm (thickness) × 1.76 mm (width) × 5.42 mm (length). The cross-sectional area of dog bone-shaped specimens was determined at its narrowest region at three different locations using a digital caliper (Digimatic 500-196-30, Mitutoyo, Japan). PHT scaffold static tensile test samples were fabricated according to the 3D CAD model. Acellular dermal matrix (ADM; GraftJacket™), which is used in clinical repair of rotator cuff injuries was cut into rectangular specimens of 10 mm (length) × 10 mm (width) × 1.20 mm (thickness). Suture retention samples were fabricated as rectangular specimens of 15 mm (length) × 5 mm (width) × 1 mm (thickness).

5.2.1. Static tensile testing

Static tensile testing was performed by first preloading PHT polymer samples to 5 N followed by uniaxially loading at a rate of 0.1 mm per second until failure. Tensile strength was defined as the tensile stress at which the PHT polymer samples break. Tensile modulus was defined as

the initial linear slope of the stress-strain curve and calculated from 0% to 2% strain. Strain-at-failure was defined as the percentage of strain change of the PHT samples when loaded to break. Total work-to-failure was calculated as the total area under the force-displacement curve. Tensile toughness was calculated as the total area under the stress-strain curve. For the tensile test with 3D-printed PHT scaffold, the PHT scaffold was pre-drilled with 4 holes at each side and two knots were tied with FiberWire suture (4-0) (AR-7230-01, Arthrex, Inc. US). The same knots were tied at the two sides of the ADM samples. Samples were loaded until failure (pull out from the suture). Ultimate load was defined as the maximum load before or at failure. Total work-to-failure was defined as the total area under the load-displacement curve.

5.2.2. Cyclic tensile testing

Cyclic tensile testing was performed by loading PHT polymer samples sinusoidally from 0.2 to 3 MPa for 10,000 cycles at 1 Hz. The lower and higher loading stress were estimated to be the passive tension and around 75% of the maximum stress generated by supraspinatus muscle [25,101]. The ultimate strain was defined as the percentage of strain change of the PHT samples after loading for 10,000 cycles. The dynamic modulus was defined as the ratio of the stress range to strain range of the hysteresis loop for a given loading cycle. The storage modulus was defined as the dynamic modulus multiplied by the cosine of the loss angle. The loss modulus was defined as the dynamic modulus multiplied by the sine of the loss angle.

5.2.3. Static creep testing

Static creep testing was performed by loading PHT polymer and ADM samples to 3 MPa and holding specimens under tension for 30 min, followed by rapid unloading to 0 MPa and monitoring of recovery for 10 min. Static creep was defined as the changes in strain (in percentage) between the initial and final time points during the 30 min holding at 3 MPa. Creep recovery was defined as the percentage change in strain after the 10 min recovery period at 0 MPa compared to the strain after holding at 3 MPa for 30 min.

5.2.4. Suture retention testing

Suture retention was performed on PHT polymer samples with 4 h post-heat curing (4h-PHT) and ADM samples. A suture hole was created 3 mm from the edge of the samples using a Micromot pen drill (MNT-070309, Proxxon, Germany) equipped with a 0.45 mm drill bit. FiberWire (4-0, Arthrex Inc., USA) was passed through the suture hole and secured in a 5 cm diameter loop using a simple, interrupted suture pattern. ADM samples were soaked in saline for 10 min prior to testing. All the samples were preloaded to 0.1 N, and then uniaxially loaded at a rate of 0.1 mm per second until failure. Fiberwire suture migration at 15 N was calculated during load-to-failure.

5.3. Ex vivo degradation and swelling of PHT polymer

5.3.1. Accelerated degradation studies

Accelerated degradation studies were performed on PHT polymer samples and ADM samples using similar geometry (type V dog bone-shaped specimen) under alkaline, acidic, and oxidizing conditions. PHT (mass of ≈300 mg) and ADM (mass of ≈70–90 mg) samples were weighed and placed separately in the following solutions with approximately 1:40 mass-to-volume ratio at room temperature for 5 days: (1) 5 N NaOH, (2) 2 N HCl (Duksan, Korea), and for 1 week: (3) 30% H_2O_2 (Merck, Germany). These reagents simulated body fluids under neutral (HBSS), alkaline (sodium hydroxide), acidic (hydrochloric acid), and oxidizing (hydrogen peroxide) conditions and have been previously used in similar studies [25]. No media change was performed during the incubation. After 1 week, wet and dry weights of PHT samples were recorded. For ADM samples, only dry weights were recorded. To obtain dried specimens, all the samples were washed in deionized water for 1 h and placed under low vacuum in a desiccating chamber overnight. By visual inspection, this drying procedure did not affect the mass of PHT or ADM samples. The amount of degradation was determined by calculating the percentage of remaining dry mass relative to its original mass. After sample drying, static tensile testing was performed for 2 N HCl-incubated PHT and ADM samples as described in Section 5.2. Samples were normalized to pristine PHT and ADM samples to determine percentage changes in tensile strength, tensile modulus and failure strain.

5.3.2. Swelling studies

Swelling studies were performed on PHT polymer samples under aqueous, alkaline and acidic conditions. PHT (mass of ≈300 mg) samples were placed separately in 10 mL and 5 mL of the following solutions at room temperature for 4 h: (1) HBSS (ThermoFisher, USA), (2) 5 N NaOH, and (3) 1 N HCl (Duksan, Korea). Swelling ratios of PHT samples after immersion at the 4 h time point were determined by calculating the ratio between wet and dry weights.

5.4. Ex vivo growth factor retention/release from 3D-printed PHT scaffold

Retention/Release profile of FGF-2 and TGF-β3 from fibrin gels embedded within PHT scaffold was assessed *ex vivo* using ELISA kits according to the manufacturer's instructions. Fibrin gel were prepared as follows: 0.15 mL of soluble fibrinogen solution (20 mg/mL, Enzyme Research Laboratories, USA) and 0.024 mL α-thrombin (8 U/mL, Enzyme Research Laboratories, USA) were mixed simultaneously with 3 μg FGF-2 (1 mg/mL), 0.6 μg TGF-β3 (0.2 mg/mL), and 0.12 mL PBS to form the 0.3 mL fibrin gel within the central porous regions of PHT scaffold at 37 °C for 30 min. Once formed, PHT scaffolds containing fibrin hydrogel were immersed in 3 mL PBS in a 12-well plate. The plate was kept at 37 °C and samples (0.25 mL) were collected with media replenishment at the following time points (1, 2, 4, 8 and 24 h, day 2, 4, 6, 8, 10, 12 and 14) and stored at −80 °C immediately. The whole plate was sealed with parafilm to minimize solution evaporation at 37 °C during the 14-day assessment period. Lastly, the amount of released FGF-2 and TGF-β3 in the PBS was determined by ELISA kits (Abcam, USA, #ab246531 and #ab272203) according to the manufacturer's instructions. The concentration, cumulative mass and cumulative percentage of ELISA-detectable FGF-2 and TGF-β3 at different time points were calculated.

5.5. In vitro characterization of 3D-printed PHT scaffold

5.5.1. Cell culture

Two different types of cells were used to model stem/progenitor cells for *in vitro* studies. Multipotent mouse C2C12 myoblasts (ATCC® CRL-1772™, Manassas, VA, US) were cultured in Dulbecco's modified Eagle's media (DMEM, Thermo Fisher Scientific Inc.) with 10% fetal bovine serum (FBS; Thermo Fisher Scientific Inc.) and 1% penicillin-streptomycin (PS, 10,000 U/mL, Fisher Scientific). Poietics™ human mesenchymal stem cells (hMSCs) (PT-2501, Lonza Walkersville Inc. MD) were cultured with mesenchymal stem cell growth medium (MSCGM™ BulletKit™, PT-3001, Lonza Walkersville Inc. MD). All the cells were kept at 37 °C, 5% CO_2 in a humidified incubator. No mycoplasma contamination was found in cell cultures, which was monitored using a mycoplasma detection kit (Nanjing Vazyme Biotech Co., Ltd. China, MycoBlue, #D101-02) and Hoechst 33342 (Anaspec, USA) staining.

5.5.2. Cell attachment assay

Cell attachment assays were performed as similarly described [71]. C2C12 cells and hMSCs were seeded into low cell attachment polystyrene 48-well plates (SPL Life Sciences, South Korea, SPL-32048) containing circular 2h-, 4h-, and 8h-PHT polymer samples (8 mm diameter and 0.6 mm height) at a density of 13.3×10^4 cells per cm^2 followed by cell counting at 3 h post-seeding. To count cells, wells were

gently washed with PBS to remove unattached cells, then incubated with 0.2 mL of 0.05% Trypsin-EDTA (ThermoFisher, USA) for 15 min to detach cells. Subsequently, 0.5 mL of growth medium was added to inhibit the actions of trypsin and cell number was counted using a hemocytometer. Cell counts were normalized to the available surface area of PHT polymer samples.

5.5.3. Cell viability assay

C2C12 cell and hMSC viability was determined using Live/Dead staining kit (Thermofisher, USA, #L3224) as previously described [71]. Cells were seeded in 24-well plates containing circular 2h-, 4h-, and 8h-PHT polymer samples (8 mm diameter and 0.6 mm height) at a density of 0.5×10^4 cells per cm^2 for C2C12 cells and 2.5×10^4 cells per cm^2 for hMSCs in their respective growth medium. Medium was changed after overnight seeding and every 48 h thereafter. Live/Dead assay was performed on day 3. Cells cultured on tissue culture-grade polystyrene (TCPS) without PHT polymer and cells treated with 70% ice-cold methanol were stained as positive and negative controls, respectively. Fluorescence images were acquired with Olympus IX83-ZDC Inverted Microscope (Olympus Corporation, Tokyo, Japan) equipped with a metal halide light source (Excelitas Technologies, USA, X-Cite 120 PC), GFP- and Cy3-equivalent Olympus IX83 FL Chroma filter sets, and a DP80 Double-CCD monochrome/colour camera.

5.5.4. Scanning electron microscopy (SEM)

SEM was performed using a Hitachi SU8010 Scanning Electron Microscope (Hitachi High-Technologies Corporation, Japan) as similarly described [29]. PHT scaffold samples (approximately 5 mm × 5 mm) with or without hMSCs (cultured for 48 h) were fixed with 2.5% glutaraldehyde (Electron Microscopy Sciences, USA). After thorough washing with 0.1 M Sorensen's phosphate buffer, pH 7.2, the samples were post-fixed in 1 % osmium tetroxide for 30 min and rinsed three times in distilled water (10 min each time). The specimens were dehydrated in a graded ethanol series, critically point dried with CO_2, and sputter coated with gold-palladium before SEM observation. Images of PHT scaffold were acquired using a Hitachi SU8000 Cold Field Scanning Electron Microscope (Hitachi High-Tech, Japan) and images with low magnification mode (30 × – 2000 ×) and high (400 × – 800,000 ×) magnification were captured using PE-PC SEM software (Hitachi High-Tech).

5.5.5. Tenogenic differentiation assay

Tendon differentiation was assessed using hMSCs cultured under tenogenic conditions followed by Picrosirius Red staining for total collagen and immunofluorescence staining for tendon-associated markers Scleraxis (Scx), Collagen type I (Col I), Tenacin C (Tnc) and Tenomodulin (Tnmd) at various timepoints as previously described [29,38,39]. PHT polymer in MSCGM medium with the supplement of growth factors and performed with Picrosirius Red staining for total collagen expression at day 10, immunofluorescence staining for Scleraxis (Scx) at day 4 and Collagen type I (Col I), Tenacin C (Tnc) and Tenomodulin (Tnmd) at day 10. hMSCs were seeded in 48-well plates containing circular 2h-, 4h-, and 8h-PHT polymer samples (8 mm diameter and 0.6 mm height) at a density of 6.6×10^4 cells per cm^2 in growth medium (MSCGM). The following day (Day 0), medium was changed to either control (MSCGM) or tenogenic differentiation medium (MSCGM with 50 ng/mL FGF-2, 10 ng/mL TGF-β3, and 50 μg/ml ascorbic acid, and changed every 72 h afterwards. On day 4 (Scx) or day 10 (Picrosirius Red, Col I, Tnc, and Tnmd), cells were fixed with 4% paraformaldehyde (Sigma Aldrich, USA) for 15 min and washed with PBS twice. Picrosirius Red staining was performed by incubating samples with 0.1 % Picrosirius Red (Sigma Aldrich, USA, Direct Red 80, #365548) for 1 h to visualize the collagenous matrix and then washed in two changes of acidified water (0.5% acetic acid) followed by a quick wash in tap water. Immunofluorescence staining were performed by blocking samples with 10% donkey serum (Jackson Immunoresearch, USA) at RT for 1 h followed by overnight incubation at 4 °C with primary antibodies, which included rabbit polyclonal anti-collagen I antibody (COL1; Abcam, USA, #ab21286) rabbit polyclonal scleraxis antibody (SCX; Abcam, USA, #ab58655), rabbit recombinant monoclonal anti-tenascin antibody (TNC; Abcam, USA, #ab108930), and rabbit polyclonal anti-tenomodulin (TNMD; Abcam, USA, Abcam, #ab203676). The following day, samples were incubated with donkey anti rabbit IgG (H + L) highly cross adsorbed, Alexa Fluor 647 (Thermofisher, USA) secondary antibody at RT for 1 h. Fluorescence images were acquired with Olympus IX83-ZDC Inverted Microscope (Olympus Corporation, Tokyo, Japan) equipped with a metal halide light source (Excelitas Technologies, USA, X-Cite 120 PC), Cy5-equivalent Olympus IX83 FL Chroma filter sets, and a DP80 Double-CCD monochrome/colour camera.

5.6. In vivo characterization of 3D-printed PHT scaffold

5.6.1. Mouse dorsal subcutaneous implantation

Mouse subcutaneous implantation surgeries were performed as previously described [40]. The study was performed according to the guidelines established by The Chinese University of Hong Kong's Animal Experimentation Ethics Committee (approved protocol: 18/211/MIS-5-C). Wild-type C57BL/6 mice (both male and female) from 8 to 12 weeks old were used and maintained in a 12:12 h light-dark cycle with free access to standard laboratory food as well as water and housed for one week before surgery.

In brief, mice were anesthetized by inhalation with isoflurane (4% for induction, 2% for maintenance) and oxygen (0.6 L/min) followed by subcutaneous injection of 0.05 mg/kg buprenorphine (Bupaq, Richter Pharma, Austraia) and 25 mg/kg cephalexin (Santa Cruz Biotechnology, USA) as an analgesic and anti-infective, respectively. The surgical area was shaved and disinfected with alternating applications of betadine and 70% alcohol. Using aseptic technique, a 2-cm incision was made on the dorsal skin with a surgical scalpel and subcutaneous pockets were created using a blunt scissors. Thereafter 3D-printed PHT scaffold (14 × 6.5 × 14 mm) was implanted on one side/flank of the body and ADM of similar size (10 × 10 × 1.20 mm) on the other side/flank. The PHT scaffold and ADM were sutured to the skin subcutaneously with 4-0 nylon sutures. After surgery, mice were allowed to recover on a heating pad and allowed free-cage activity. Buprenorphine (0.05 mg/kg) was administered subcutaneously twice a day for 2 days for post-operative analgesia. At 3-week post-surgery, mice were euthanized via carbon dioxide overdose. Skin samples with PHT scaffold and ADM were collected for histological analysis.

5.6.2. Mouse subcutaneous implantation histology

Histological analysis was performed on paraffin-embedded and sectioned mouse subcutaneous implantation samples as previously described [40,71]. Freshly harvested samples were fixed in 4% paraformaldehyde for 24 h. To produce paraffin embedded tissue blocks, samples were dehydrated through a graded ethanol series (50%, 70%, 90%, 95% and 100% ethanol, 1 h for each wash at 25 °C), washed with xylene, and infiltrated with paraffin at 60 °C under vacuum. Paraffin-embedded samples were sectioned at 5 μm using a Leica RM2235 microtome (Leica Biosystems, Germany), deparaffinized, rehydrated, and processed for H&E and immunohistochemical staining.

For H&E staining, the protocol was performed according to manufacturer's instructions (Electron Microscopy Science, USA). Histological images were acquired with Olympus IX83-ZDC Inverted Microscope (Olympus Corporation, Japan) equipped with a DP80 Double-CCD monochrome/colour camera.

For immunohistochemical staining, CD68 and iNOS were detected using the VECTASTAIN® ABC-HRP Kit (Vector Laboratories, Inc. United States) and Pierce™ DAB Substrate Kit (Thermofisher, USA). In brief, deparaffinized and rehydrated sections were incubated in 10 mM sodium citrate buffer (pH 6.0) at 98 °C for 20 min for antigen retrieval. Thereafter, sections were blocked with 10% goat serum for 30 min

followed by incubation with primary antibodies including mouse anti-CD68 and rabbit anti-iNOS (1:200, Arigo Biolaboratories Corp., Taiwan) at 4 °C overnight, followed by biotinylated goat anti-mouse IgG antibody for 30 min and ABC-HRP reagent for 30 min at RT prior to staining with DAB reagents. Histological images were acquired with Olympus IX83-ZDC Inverted Microscope (Olympus Corporation, Japan) equipped with a DP80 Double-CCD monochrome/colour camera.

5.6.3. Rabbit large-to-massive rotator cuff injury

Rabbit rotator cuff injury was performed according to the guidelines established by The Chinese University of Hong Kong's Animal Experimentation Ethics Committee (approved protocol: 18/006/ECS and 21-160-GRF). New Zealand White rabbits (both male and female) from 3 to 4 months old with body weight of 3.2–4 kg were used in the current study and maintained in a 12:12 h light-dark cycle with free access to standard laboratory food as well as water and housed for one week before surgery. The rabbits were randomly divided into two groups, PHT only and PHT with low dose growth factors (PHT-GFs). Both gender and the surgical side were randomized. The contralateral side was used as an uninjured, no surgery control. 3D-printed PHT scaffold was prepared similarly as described in 'Synthesis of PHT polymer'.

In brief, rabbits were initially anesthetized by intramuscular injection of 35 mg/kg ketamine (10%) and 5 mg/kg xylazine (2%) with a supplemental dose of 10 mg/kg Ketamine (10%) and 3 mg/kg Xylazine (2%) via a cannulated ear vein every 20 min as needed. Subcutaneous injection of 0.05 mg/kg buprenorphine (Bupaq, Richter Pharma, Austria) and 20 mg/kg cephalexin (Santa Cruz Biotechnology, USA) was administered as an analgesic and anti-infective, respectively. Rabbits were placed on a covered heating pad during surgery to maintain body temperature. The surgical area was shaved and disinfected with alternating applications of betadine and 70% alcohol. Using aseptic technique, a 3-cm longitudinal skin incision was made above the humerus head and the rotator cuff tissue was exposed. As an intraoperative analgesic, 2 mg/kg bupivacaine was locally infiltrated. Thereafter, the triceps muscle and the deltoid muscle were split to identify and isolate the supraspinatus muscle and supraspinatus tendon (SST). To introduce a tendon segmental defect and prepare for graft implantation, the SST was first pre-loaded with 4-0 non-absorbable FiberWire® sutures (Arthrex, USA, #AR-7230-01) using the continuous lock suture technique, which were passed through the SST tendon at its proximal and distal ends about 7 mm apart (leaving four long suture arms at each side), and followed by removal of a 3 mm length of tendon between the SST proximal and distal ends. The defect was then immediately repaired by passing the long arms of the sutures through 3D-printed PHT scaffold containing fibrin hydrogel with or without growth factors (FGF-2 and TGF-β3). Square knots were tied on the top and bottom faces of 3D-printed PHT scaffold for secure attachment with the proximal and distal SST defect margins. Fibrin hydrogel was formed within the central porous regions of PHT scaffold just prior to surgery by addition of 0.15 mL of soluble fibrinogen solution (20 mg/mL, Enzyme Research Laboratories, USA), 0.024 mL α-thrombin (8 U/mL, Enzyme Research Laboratories, USA), and about 0.12 mL PBS with or without growth factors (3 μg FGF-2 and 0.6 μg TGF-β3) at 37 °C for 30 min. The deltoid muscle and skin were re-approximated and closed with 4-0 absorbable Polysorb™ suture (eSutures, USA) and 4-0 nylon suture (eSutures, USA), respectively. After surgery, rabbits were allowed to recover on a heating pad and allowed free-cage activity. Buprenorphine (0.05 mg/kg) was administered subcutaneously twice a day for 2 days for post-operative analgesia. At 8 weeks post-surgery, rabbits were euthanized via intramuscular overdose of pentobarbital. The supraspinatus muscle-tendon-bone units were collected for biomechanical (n = 8 for each group) and histological analysis (n = 6 for each group).

5.6.4. Rabbit rotator cuff tensile testing

Harvested supraspinatus muscle-tendon-bone tissue samples were biomechanically tested using an ADMET mechanical tester (ADMET, USA) equipped with a 100 lb (445 N) load cell with data analyzed using Microsoft Excel (Microsoft Corporation, USA) as similarly described [25].

The supraspinatus muscle-tendon-bone units were freshly harvested, wrapped in gauze, moistened with PBS solution, and stored at −20 °C until tensile testing. On the day of testing, SST sample with humerus head was isolated by careful dissection. The humerus head was mounted onto a custom holder that was gripped on one end while the tendon end was gripped on the other end using 60-Grit sandpaper. The whole setup was immersed in a 37 °C saline-containing water bath before and during testing. Humeral bone-SST samples were preloaded to 5 N, and then uniaxially loaded at a rate of 0.25 mm per second (1% strain per second) until failure. Ultimate load, stiffness (N/mm), ultimate displacement and total work-to-failure were recorded and calculated. All the values were normalized to the contralateral uninjured (no surgery) limb.

5.6.5. Rabbit rotator cuff histology

Histological analysis was performed on paraffin-embedded and sectioned rabbit tissue samples as similarly described [25,40,71]. Freshly harvested samples were fixed in 4% paraformaldehyde for 72–96 h at 4 °C and further decalcified in 10% EDTA, pH7.4 (Sigma Aldrich, USA) for 3–4 weeks. To produce paraffin embedded tissue blocks, samples were dehydrated through a graded ethanol series (50%, 70%, 90%, 95% and 100% ethanol, 1 h for each wash at 25 °C), washed with xylene, and infiltrated with paraffin at 60 °C under vacuum. Paraffin-embedded samples were sectioned at 16 μm using a Leica RM2235 microtome (Leica Biosystems, Germany). To transfer large tissue sections, an adaptation of the Kawamoto film method was adopted in which sections were transferred by a 3 M tape to a glass slide freshly coated with adhesive glue (Norland Optical Adhesive NOA 63) and subjected to UV exposure for 20 s. Thereafter, sections were deparaffinized, rehydrated, and processed for H&E, Picrosirius Red, and trichrome staining as well as immunofluorescence staining.

For H&E, Picrosirius Red, and Masson's Trichrome staining, the protocols were performed according to manufacturer's instructions (Electron Microscopy Science, USA). Macroscopic and microscopic scoring were performed with H&E images using the self-defined parameters (Tables S4 and S5) modified based on the revised Bonar score [102]. The scoring was done by at least two individuals that were familiar with tendon morphology and histology but were blinded as to the grouping information for each sample. For collagen quantification, signal intensity from a defined region of interest (ROI) from Picrosirius Red-stained brightfield images were measured by using the image histogram tool of Adobe Photoshop 20.01 software to determine average pixel intensity (Adobe Inc., USA). Collagen alignment was analyzed by quantify the orientation and anisotropy of fiber arrays of the ROI in polarized light image by FibrilTool of NIH ImageJ plug-in Ref. [103]. Histological images were acquired with Zeiss Axioscan 7 Automatic Slide Scanner (ZEISS, Germany) equipped with Colibri 7 Type RGB-UV and illuminator VIS-LED and Axiocam 705 colour camera (for large-scale images) and Olympus IX83-ZDC Inverted Microscope (Olympus Corporation, Japan) equipped with a DP80 Double-CCD monochrome/colour camera.

For immunofluorescence staining, the protocol was performed as previously described with minor modifications [39,40,71]. In brief, rehydrated sections were first incubated in 0.1% trypsin at 37 °C for 30 min and Tris-EDTA buffer (pH 9.0) at 98 °C for 20 min for antigen retrieval. Thereafter, sections were washed three times in wash buffer (PBS and 0.1% BSA), blocked with 10% donkey serum (Jackson Immunoresearch, USA) for 1 h at 25 °C, followed by incubation with primary antibodies at 4 °C overnight. Primary antibodies included goat anti-type I collagen-UNLB (Col1, 4 μg/mL, SouthernBiotech, USA, #1310-01), mouse anti-Scleraxis (A-7) (Scx, 2 μg/mL, Santa Cruz Biotechnology, USA, #sc-518082), rabbit anti- Tenomodulin (Tnmd, 2 μg/mL, Abcam, USA, #ab203676). For Tnmd, tissue sections were further blocked with Background Buster (Innovex Biosciences Inc., USA,

#NB306-50). 'No primary antibody' samples were used as a negative control. Following primary antibody staining, samples were rinsed three times in wash buffer (5 min each) and incubated with secondary antibodies for 1 h at 25 °C. Secondary antibodies included Alexa 555-labeled donkey anti-goat, Alexa 647-labeled donkey anti-mouse, and Alexa 647-labeled donkey anti-rabbit secondary antibody (Thermofisher, USA). Thereafter, sections were incubated with Hoechst dye (1:5000) for 15 min, and rinsed three times in wash buffer (5 min each). Fluorescence images were acquired on a Nikon Ti2-E Inverted Fluorescence Microscope equipped with fluorescence light source (Lumencor SPECTRA III Light Engine), Hoechst- Cy3-, and Cy5-equivalent fluorescent filters, and a DP80 Double-CCD monochrome/colour camera.

5.7. Statistical analysis

Sample sizes for each experiment are indicated in each figure legend and were estimated to detect a group mean difference of 50% ± 1 to 2 standard deviations with a power (1-β) of 0.8 and $\alpha = 0.05$. Quantitative data was presented as means ± standard error of mean (mean ± SEM). Statistical significance was analyzed using SPSS Statistics 24.0 (IBM., USA) software. The Shapiro–Wilk test and the Levene test were used to determine whether the data were normally distributed and had equal variances among groups, respectively. Unpaired *t*-test was performed to determine statistical significance between two groups whereas for multiple comparisons, one-way analysis of variance (ANOVA) was performed. For one-way ANOVA, pairwise comparisons were performed using Tukey's honestly significant difference post hoc test (on data that satisfied normality or equal variance assumptions) or Dunnett T3 post hoc test (on data that did not satisfy both normality and equal variance assumptions to enable improved control of Type I error and greater power under conditions of non-normality and heterogeneity of variance). Statistical significance was established at a *p*-value of <0.05.

Data availability

Data and supporting information are available from the manuscript or from the authors upon reasonable request.

Ethics approval and consent to participate

All the animal experiments were approved and conducted according to the guidelines established by The Chinese University of Hong Kong's Animal Experimentation Ethics Committee (approved protocol: 18/211/MIS-5-C for mice and 18/006/ECS as well as 21-160-GRF for rabbit).

CRediT authorship contribution statement

Xu Zhang: Writing – original draft, Methodology, Investigation, Formal analysis, Data curation. **Ke Li:** Investigation, Formal analysis. **Chenyang Wang:** Investigation, Formal analysis. **Ying Rao:** Investigation, Formal analysis. **Rocky S. Tuan:** Writing – review & editing, Investigation, Funding acquisition. **Dan Michelle Wang:** Writing – review & editing, Validation, Investigation, Funding acquisition, Formal analysis. **Dai Fei Elmer Ker:** Writing – review & editing, Writing – original draft, Validation, Supervision, Resources, Project administration, Funding acquisition, Conceptualization.

Declaration of competing interest

The authors declare the following financial interests/personal relationships which may be considered as potential competing interests:

Dai Fei Elmer Ker reports financial support was provided by Hong Kong Health Bureau. Dan Michelle Wang reports financial support was provided by Hong Kong Health Bureau. Dai Fei Elmer Ker reports financial support was provided by Hong Kong Research Grants Council. Dan Michelle Wang reports financial support was provided by Hong Kong Research Grants Council. Dan Michelle Wang reports financial support was provided by National Natural Science Foundation of China-Hong Kong Research Grants Council Joint Research Scheme. Dai Fei Elmer Ker reports financial support was provided by Hong Kong Innovation and Technology Commission. Dan Michelle Wang reports financial support was provided by Hong Kong Innovation and Technology Commission. Rocky S. Tuan reports financial support was provided by Hong Kong Innovation and Technology Commission. Dai Fei Elmer Ker has patent pending to The Chinese University of Hong Kong. Xu Zhang has patent pending to The Chinese University of Hong Kong. Dan Michelle Wang has patent pending to The Chinese University of Hong Kong. Co-author is serving as an editorial board member for the journal to which we are submitting: D.M.W. If there are other authors, they declare that they have no known competing financial interests or personal relationships that could have appeared to influence the work reported in this paper. Dan Michelle Wang is an editorial board member for *Bioactive Materials* and was not involved in the editorial review or the decision to publish this article.

Acknowledgements

The authors would also like to thank the School of Biomedical Sciences Core Facility and Laboratory Animal Services Centre (LASEC) from The Chinese University of Hong Kong for use of their equipment and facilities as well as their staff's technical assistance. This work was supported by Hong Kong Health Bureau (DFEK: Health Medical and Research Fund, 08190466; DMW: Health Medical and Research Fund, 07180686), Hong Kong Research Grants Council (DFEK: Early Career Scheme Award, 24201720; General Research Fund: 14213922; DMW: General Research Fund: 14118620 and 14121121), National Natural Science Foundation of China-Hong Kong Research Grants Council Joint Research Scheme (DMW: N_CUHK409/23), Hong Kong Innovation and Technology Commission (DFEK: Tier 3 Award, ITS/090/18; DW: ITS/333/18; DFEK, DMW, and RST: Health@InnoHK program), and The Chinese University of Hong Kong (DFEK: Faculty Innovation Award, FIA2018/A/01). The support of the Lee Quo Wei and Lee Yick Hoi Lun Professorship in Tissue Engineering and Regenerative Medicine (RST) is also gratefully acknowledged.

Appendix A. Supplementary data

Supplementary data to this article can be found online at https://doi.org/10.1016/j.bioactmat.2024.03.036.

References

[1] D. Wang, X. Zhang, S. Huang, et al., Engineering multi-tissue units for regenerative medicine: bone-tendon-muscle units of the rotator cuff, Biomaterials 272 (2021) 120789.
[2] X. Zhang, D. Wang, K.K. Mak, et al., Engineering musculoskeletal grafts for multi-tissue unit repair: Lessons from developmental biology and wound healing, Front. Physiol. 12 (2021) 691954.
[3] X. Zhang, D. Wang, Z. Wang, et al., Clinical perspectives for repairing rotator cuff injuries with multi-tissue regenerative approaches, J Orthop Translat 36 (2022) 91–108.
[4] M.C.P. Vila Pouca, M.P.L. Parente, R.M.N. Jorge, et al., Injuries in muscle-tendon-bone units: a systematic review considering the role of passive tissue fatigue, Orthop J Sports Med 9 (8) (2021) 23259671211020731.
[5] S.A. Shah, I. Kormpakis, N. Havlioglu, et al., Sclerostin antibody treatment enhances rotator cuff tendon-to-bone healing in an animal model, J Bone Joint Surg Am 99 (10) (2017) 855–864.
[6] U.G. Longo, A. Mazzola, F. Magri, et al., Histological, radiological and clinical analysis of the supraspinatus tendon and muscle in rotator cuff tears, BMC Muscoskel. Disord. 24 (1) (2023) 127.
[7] R.C. Mather 3rd, L. Koenig, D. Acevedo, et al., The societal and economic value of rotator cuff repair, J Bone Joint Surg Am 95 (22) (2013) 1993–2000.
[8] H. Xiao, B. Wen, D. Yan, et al., Hot spots and frontiers in bone-tendon interface research: a bibliometric analysis and visualization from 2000 to 2023, Front Surg 10 (2023) 1326564.
[9] O. Mani, A.M. Nucci, M. Scaglione, et al., Bibliometric trend analysis in a decade of european orthopaedic literature, Acta Biomed. 92 (3) (2021) e2021280.

[10] A. Alhaskawi, H. Zhou, Y. Dong, et al., Advancements in 3D-printed artificial tendon, J. Biomed. Mater. Res. B Appl. Biomater. 112 (2) (2024) e35364.
[11] E. Itoi, L.J. Berglund, J.J. Grabowski, et al., Tensile properties of the supraspinatus tendon, J. Orthop. Res. 13 (4) (1995) 578–584.
[12] T. Matsuhashi, A.W. Hooke, K.D. Zhao, et al., Tensile properties of a morphologically split supraspinatus tendon, Clin. Anat. 27 (5) (2014) 702–706.
[13] G.A. Lichtwark, A.M. Wilson, Is achilles tendon compliance optimised for maximum muscle efficiency during locomotion? J. Biomech. 40 (8) (2007) 1768–1775.
[14] M. Rickert, H. Georgousis, U. Witzel, Tensile strength of the tendon of the supraspinatus muscle in the human. A biomechanical study, Unfallchirurg 101 (4) (1998) 265–270.
[15] S. Rawson, S. Cartmell, J. Wong, Suture techniques for tendon repair: a comparative review, Muscles Ligaments Tendons J 3 (3) (2013) 220–228.
[16] U.G. Longo, F. Franceschi, L. Ruzzini, et al., Histopathology of the supraspinatus tendon in rotator cuff tears, Am. J. Sports Med. 36 (3) (2008) 533–538.
[17] K.S. Miller, B.K. Connizzo, E. Feeney, et al., Examining differences in local collagen fiber crimp frequency throughout mechanical testing in a developmental mouse supraspinatus tendon model, J. Biomech. Eng. 134 (4) (2012) 041004.
[18] A.J. Rosenbaum, J.F. Wicker, J.S. Dines, et al., Histologic stages of healing correlate with restoration of tensile strength in a model of experimental tendon repair, HSS J. 6 (2) (2010) 164–170.
[19] L.M. Galatz, C.M. Ball, S.A. Teefey, et al., The outcome and repair integrity of completely arthroscopically repaired large and massive rotator cuff tears, J Bone Joint Surg Am 86 (2) (2004) 219–224.
[20] S.J. Kim, S.H. Kim, S.K. Lee, et al., Arthroscopic repair of massive contracted rotator cuff tears: Aggressive release with anterior and posterior interval slides do not improve cuff healing and integrity, J Bone Joint Surg Am 95 (16) (2013) 1482–1488.
[21] G.G. Ellman H, Open repair of full thickness rotator cuff tears, in: H. Ellman (Ed.), Arthroscopic Shoulder Surgery and Related Procedures, Lea & Febiger, Philadelphia, 1993, pp. 181–202.
[22] I. Santos, L. Pichler, M.M. Saller, et al., Effect of shape and size of supraspinatus tears on rotator cuff strain distribution: an in vitro study, J. Shoulder Elbow Surg. 32 (2) (2023) e71–e83.
[23] K.J. Lee, Y.T. Kim, M. Choi, et al., Characteristics and outcomes of l-shaped and reverse l-shaped rotator cuff tears, Bone Joint Lett. J 104-B (3) (2022) 394–400.
[24] J. Laskovski, J. Abrams, A. Bogdanovska, et al., Arthroscopic rotator cuff repair with allograft augmentation: Making it simple, Arthrosc Tech 8 (6) (2019) e597–e603.
[25] D.F.E. Ker, D. Wang, A.W. Behn, et al., Functionally graded, bone- and tendon-like polyurethane for rotator cuff repair, Adv. Funct. Mater. 28 (20) (2018) 1707107.
[26] F.X.W. Robert, M. Silverstein, David J. Kiemle, in: Spectrometric Identification of Organic Compounds, seventh ed., John Wiley & Sons, Hoboken, NJ, 2005.
[27] L.S. Teo, C.Y. Chen, J.F. Kuo, Fourier transform infrared spectroscopy study on effects of temperature on hydrogen bonding in amine-containing polyurethanes and poly(urethane-urea)s, Macromolecules 30 (6) (1997) 1793–1799.
[28] Sigma Aldrich, IR Spectrum Table & Chart, Online, Sigma Aldrich, St. Louis, USA, 2023. Available from: URL: https://www.sigmaaldrich.com/HK/en/technical-documents/technical-article/analytical-chemistry/photometry-and-reflectometry/ir-spectrum-table.
[29] K. Li, X. Zhang, D. Wang, et al., Synergistic effects of growth factor-based serum-free medium and tendon-like substrate topography on tenogenesis of mesenchymal stem cells, Biomater. Adv. 146 (2023) 213316.
[30] S. Chaudhury, C. Holland, M.S. Thompson, et al., Tensile and shear mechanical properties of rotator cuff repair patches, J. Shoulder Elbow Surg. 21 (9) (2012) 1168–1176.
[31] W. Kong, C. Wang, C. Jia, et al., Muscle-inspired highly anisotropic, strong, ion-conductive hydrogels, Adv. Mater. 30 (39) (2018) e1801934.
[32] M.T.I. Mredha, Y.Z. Guo, T. Nonoyama, et al., A facile method to fabricate anisotropic hydrogels with perfectly aligned hierarchical fibrous structures, Adv. Mater. 30 (9) (2018) 201704937.
[33] M. Sun, H. Li, Y. Hou, et al., Multifunctional tendon-mimetic hydrogels, Sci. Adv. 9 (7) (2023) eade6973.
[34] C.A. Cummins, R.C. Appleyard, S. Strickland, et al., Rotator cuff repair: an ex vivo analysis of suture anchor repair techniques on initial load to failure, Arthroscopy 21 (10) (2005) 1236–1241.
[35] H. Kim, S.B. Han, H.S. Song, Suture slippage after arthroscopic cuff repair: medial displacement of suture knots on follow-up ultrasonography, Orthop J Sports Med 9 (8) (2021) 23259671211021820.
[36] J. Taipale, J. Keski-Oja, Growth factors in the extracellular matrix, Faseb. J. 11 (1) (1997) 51–59.
[37] M.M. Martino, P.S. Briquez, A. Ranga, et al., Heparin-binding domain of fibrin (ogen) binds growth factors and promotes tissue repair when incorporated within a synthetic matrix, Proc. Natl. Acad. Sci. U.S.A. 110 (12) (2013) 4563–4568.
[38] D.F.E. Ker, A.S. Nain, L.E. Weiss, et al., Bioprinting of growth factors onto aligned sub-micron fibrous scaffolds for simultaneous control of cell differentiation and alignment, Biomaterials 32 (32) (2011) 8097–8107.
[39] D.F.E. Ker, B. Chu, J.A. Phillippi, et al., Engineering spatial control of multiple differentiation fates within a stem cell population, Biomaterials 32 (13) (2011) 3413–3422.
[40] D. Wang, D.F.E. Ker, K.W. Ng, et al., Combinatorial mechanical gradation and growth factor biopatterning strategy for spatially controlled bone-tendon-like cell differentiation and tissue formation, NPG Asia Mater. 13 (1) (2021) 26.
[41] I. Ding, A.M. Peterson, Half-life modeling of basic fibroblast growth factor released from growth factor-eluting polyelectrolyte multilayers, Sci. Rep. 11 (1) (2021) 9808.
[42] I. Ding, D.M. Shendi, M.W. Rolle, et al., Growth-factor-releasing polyelectrolyte multilayer films to control the cell culture environment, Langmuir 34 (3) (2018) 1178–1189.
[43] S. Premaraj, B.L. Mundy, D. Morgan, et al., Sustained delivery of bioactive cytokine using a dense collagen gel vehicle collagen gel delivery of bioactive cytokine, Arch. Oral Biol. 51 (4) (2006) 325–333.
[44] J.A. Parker, G. Brunner, X.F. Walboomers, et al., Release of bioactive transforming growth factor beta(3) from microtextured polymer surfaces in vitro and in vivo, Tissue Eng. 8 (5) (2002) 853–861.
[45] Y. Ozasa, A. Gingery, A.R. Thoreson, et al., A comparative study of the effects of growth and differentiation factor 5 on muscle-derived stem cells and bone marrow stromal cells in an in vitro tendon healing model, J Hand Surg Am 39 (9) (2014) 1706–1713.
[46] S.G. Park, B.J. Shim, H.G. Seok, How much will high tension adversely affect rotator cuff repair integrity? Arthroscopy 35 (11) (2019) 2992–3000.
[47] Y. Ma, X. Zhang, J. Wang, et al., Effect of bone morphogenetic protein-12 gene transfer on posterior cruciate ligament healing in a rabbit model, Am. J. Sports Med. 37 (3) (2009) 599–609.
[48] N. Saveh Shemshaki, H.M. Kan, M. Barajaa, et al., Muscle degeneration in chronic massive rotator cuff tears of the shoulder: addressing the real problem using a graphene matrix, Proc. Natl. Acad. Sci. U.S.A. 119 (33) (2022) e2208106119.
[49] A. Islam, M.S. Bohl, A.G. Tsai, et al., Biomechanical evaluation of a novel suturing scheme for grafting load-bearing collagen scaffolds for rotator cuff repair, Clin. Biomech. 30 (7) (2015) 669–675.
[50] B.G. Santoni, K.C. Mcgilvray, A.S. Lyons, et al., Biomechanical analysis of an ovine rotator cuff repair via porous patch augmentation in a chronic rupture model, Am. J. Sports Med. 38 (4) (2010) 679–686.
[51] L. Du, C. Qin, H. Zhang, et al., Multicellular bioprinting of biomimetic inks for tendon-to-bone regeneration, Adv. Sci. 10 (21) (2023) e2301309.
[52] Y. Rao, C. Zhu, H.C. Suen, et al., Tenogenic induction of human adipose-derived stem cells by soluble tendon extracellular matrix: composition and transcriptomic analyses, Stem Cell Res. Ther. 13 (1) (2022) 380.
[53] G. Kaneda, J.L. Chan, C.M. Castaneda, et al., iPSC-derived tenocytes seeded on microgrooved 3D printed scaffolds for achilles tendon regeneration, J. Orthop. Res. 41 (10) (2023) 2205–2220.
[54] N. Malandain, H. Sanz-Fraile, R. Farre, et al., Cell-laden 3D hydrogels of type i collagen incorporating bacterial nanocellulose fibers, ACS Appl. Bio Mater. 6 (9) (2023) 3638–3647.
[55] M. Li, Y. Wu, T. Yuan, et al., Biofabrication of composite tendon constructs with the fibrous arrangement, high cell density, and enhanced cell alignment, ACS Appl. Mater. Interfaces 15 (41) (2023) 47989–48000.
[56] A. Hoffmann, G. Pelled, G. Turgeman, et al., Neotendon formation induced by manipulation of the smad8 signalling pathway in mesenchymal stem cells, J. Clin. Invest. 116 (4) (2006) 940–952.
[57] Y. Jiang, Y. Shi, J. He, et al., Enhanced tenogenic differentiation and tendon-like tissue formation by tenomodulin overexpression in murine mesenchymal stem cells, J Tissue Eng Regen Med 11 (9) (2017) 2525–2536.
[58] X. Zhu, Z. Liu, S. Wu, et al., Enhanced tenogenic differentiation and tendon-like tissue formation by scleraxis overexpression in human amniotic mesenchymal stem cells, J. Mol. Histol. 51 (3) (2020) 209–220.
[59] J. Lu, X. Yang, C. He, et al., Rejuvenation of tendon stem/progenitor cells for functional tendon regeneration through platelet-derived exosomes loaded with recombinant yap1, Acta Biomater. 161 (2023) 80–99.
[60] H. Wang, R. Yu, M. Wang, et al., Insulin-like growth factor binding protein 4 loaded electrospun membrane ameliorating tendon injury by promoting retention of igf-1, J. Contr. Release 356 (2023) 162–174.
[61] D. Wang, C.C.M. Pun, S. Huang, et al., Tendon-derived extracellular matrix induces mesenchymal stem cell tenogenesis via an integrin/transforming growth factor-beta crosstalk-mediated mechanism, Faseb. J. 34 (6) (2020) 8172–8186.
[62] T. Tokunaga, C. Shukunami, N. Okamoto, et al., Fgf-2 stimulates the growth of tenogenic progenitor cells to facilitate the generation of tenomodulin-positive tenocytes in a rat rotator cuff healing model, Am. J. Sports Med. 43 (10) (2015) 2411–2422.
[63] D. Kovacevic, A.J. Fox, A. Bedi, et al., Calcium-phosphate matrix with or without tgf-beta3 improves tendon-bone healing after rotator cuff repair, Am. J. Sports Med. 39 (4) (2011) 811–819.
[64] N.M. Wolfman, G. Hattersley, K. Cox, et al., Ectopic induction of tendon and ligament in rats by growth and differentiation factors 5, 6, and 7, members of the tgf-beta gene family, J. Clin. Invest. 100 (2) (1997) 321–330.
[65] J. Liu, X. Tao, L. Chen, et al., Ctgf positively regulates bmp12 induced tenogenic differentiation of tendon stem cells and signaling, Cell. Physiol. Biochem. 35 (5) (2015) 1831–1845.
[66] K. Song, T. Jiang, P. Pan, et al., Exosomes from tendon derived stem cells promote tendon repair through mir-144-3p-regulated tenocyte proliferation and migration, Stem Cell Res. Ther. 13 (1) (2022) 80.
[67] S. Cao, Y. Wei, R. Bo, et al., Inversely engineered biomimetic flexible network scaffolds for soft tissue regeneration, Sci. Adv. 9 (39) (2023) eadi8606.
[68] W. Kiratitanaporn, J. Guan, D. Berry, et al., Multimodal 3D printing for micro-modulation of scaffold stiffness via machine learning, Tissue Eng. (2023) in press.
[69] B. Shiroud Heidari, E. Muinos Lopez, E. Harrington, et al., Novel hybrid biocomposites for tendon grafts: the addition of silk to polydioxanone and poly (lactide-co-caprolactone) enhances material properties, in vitro and in vivo biocompatibility, Bioact. Mater. 25 (2023) 291–306.

[70] R.A. Sun Han Chang, J.F. Shanley, M.E. Kersh, et al., Tough and tunable scaffold-hydrogel composite biomaterial for soft-to-hard musculoskeletal tissue interfaces, Sci. Adv. 6 (34) (2020) eabb6763.
[71] D. Wang, X. Zhang, K.W. Ng, et al., Growth and differentiation factor-7 immobilized, mechanically strong quadrol-hexamethylene diisocyanate-methacrylic anhydride polyurethane polymer for tendon repair and regeneration, Acta Biomater. 154 (2022) 108–122.
[72] X. Wang, K. Xu, L. Mu, et al., Mussel-derived bioadaptive artificial tendon facilitates the cell proliferation and tenogenesis to promote tendon functional reconstruction, Adv. Healthcare Mater. 12 (24) (2023) e2203400.
[73] C. Zhu, S. Pongkitwitoon, J. Qiu, et al., Design and fabrication of a hierarchically structured scaffold for tendon-to-bone repair, Adv. Mater. 30 (16) (2018) e1707306.
[74] M. Szycher, Structure–property relations in polyurethanes, in: M. Szycher (Ed.), Szycher's Handbook of Polyurethanes, CRC Press, Boca Raton, 2012.
[75] N.B. Cramer, C.N. Bowman, Kinetics of thiol-ene and thiol-acrylate photopolymerizations with real-time fourier transform infrared, J. Polym. Sci., Polym. Chem. Ed. 39 (19) (2001) 3311–3319.
[76] J. Shin, H. Matsushima, C.M. Comer, et al., Thiol-isocyanate-ene ternary networks by sequential and simultaneous thiol click reactions, Chem. Mater. 22 (8) (2010) 2616–2625.
[77] H. Matsushima, J. Shin, C.N. Bowman, et al., Thiol-isocyanate-acrylate ternary networks by selective thiol-click chemistry, J. Polym. Sci., Polym. Chem. Ed. 48 (15) (2010) 3255–3264.
[78] D.P. Nair, M. Podgórski, S. Chatani, et al., The thiol-michael addition click reaction: a powerful and widely used tool in materials chemistry, Chem. Mater. 26 (1) (2014) 724–744.
[79] D. Ahn, L.M. Stevens, K. Zhou, et al., Additives for ambient 3D printing with visible light, Adv. Mater. 33 (44) (2021) e2104906.
[80] A. Mishra, V. Srivastava, Biomaterials and 3D printing techniques used in the medical field, J. Med. Eng. Technol. 45 (4) (2021) 290–302.
[81] U. Jammalamadaka, K. Tappa, Recent advances in biomaterials for 3D printing and tissue engineering, J. Funct. Biomater. 9 (1) (2018) 22.
[82] C. Wang, X. Zhang, D.M. Wang, et al., Optimized design of an enthesis-mimicking suture anchor-tendon hybrid graft for mechanically robust bone-tendon repair, Acta Biomater. 176 (2024) 277–292.
[83] P. Huuskonen, S.P. Porras, B. Scholten, et al., Occupational exposure and health impact assessment of diisocyanates in Finland, Toxics 11 (3) (2023) 229.
[84] T.D. Tenkate, Occupational exposure to ultraviolet radiation: a health risk assessment, Rev. Environ. Health 14 (4) (1999) 187–209.
[85] L.R. Bennison, C.N. Miller, R.J. Summers, et al., The pH of wounds during healing and infection: a descriptive literature review, Wound Pract Res 25 (2) (2017) 63–69.
[86] D.G. Metcalf, M. Haalboom, P.G. Bowler, et al., Elevated wound fluid pH correlates with increased risk of wound infection, Wound Medicine 26 (1) (2019) 100166.
[87] L.A. Schneider, A. Korber, S. Grabbe, et al., Influence of pH on wound-healing: a new perspective for wound-therapy? Arch. Dermatol. Res. 298 (9) (2007) 413–420.
[88] M.J. Smith, J.L. Cook, K. Kuroki, et al., Comparison of a novel bone-tendon allograft with a human dermis-derived patch for repair of chronic large rotator cuff tears using a canine model, Arthroscopy 28 (2) (2012) 169–177.
[89] J.A. Soler, S. Gidwani, M.J. Curtis, Early complications from the use of porcine dermal collagen implants (Permacol) as bridging constructs in the repair of massive rotator cuff tears. A report of 4 cases, Acta Orthop. Belg. 73 (4) (2007) 432–436.
[90] T.A. Wren, S.A. Yerby, G.S. Beaupre, et al., Mechanical properties of the human Achilles tendon, Clin. Biomech. 16 (3) (2001) 245–251.
[91] C. Cai, W. Wang, J. Liang, et al., Mmp-2 responsive unidirectional hydrogel-electrospun patch loading tgf-β1 sirna polyplexes for peritendinous anti-adhesion, Adv. Funct. Mater. 31 (6) (2021) 2008364.
[92] L. Du, J. Wu, Y. Han, et al., Immunomodulatory multicellular scaffolds for tendon-to-bone regeneration, Sci. Adv. 10 (10) (2024) eadk6610.
[93] S. Minkwitz, A. Schmock, A. Kurtoglu, et al., Time-dependent alterations of mmps, timps and tendon structure in human achilles tendons after acute rupture, Int. J. Mol. Sci. 18 (10) (2017) 2199.
[94] Z. Tu, Y. Zhong, H. Hu, et al., Design of therapeutic biomaterials to control inflammation, Nat. Rev. Mater. 7 (7) (2022) 557–574.
[95] J.H. Van Bilsen, J.P. Wagenaar-Hilbers, M.C. Grosfeld-Stulemeijer, et al., Matrix metalloproteinases as targets for the immune system during experimental arthritis, J. Immunol. 172 (8) (2004) 5063–5068.
[96] M. Zhang, T. Yu, J. Li, et al., Matrix metalloproteinase-responsive hydrogel with on-demand release of phosphatidylserine promotes bone regeneration through immunomodulation, Adv. Sci. (2024) e2306924.
[97] X. He, G. Gong, M. Chen, et al., Metal-phenolic nanocloaks on cancer cells potentiate sting pathway activation for synergistic cancer immunotherapy, Angew Chem. Int. Ed. Engl. 63 (12) (2024) e202314501.
[98] X. Liao, G. Gong, M. Dai, et al., Systemic tumor suppression via macrophage-driven automated homing of metal-phenolic-gated nanosponges for metastatic melanoma, Adv. Sci. 10 (18) (2023) 2207488.
[99] J. Pan, H. Liao, G. Gong, et al., Supramolecular nanoarchitectonics of phenolic-based nanofiller for controlled diffusion of versatile drugs in hydrogels, J. Contr. Release 360 (2023) 433–446.
[100] X. Qiu, X. Wang, Y. He, et al., Superstructured mesocrystals through multiple inherent molecular interactions for highly reversible sodium ion batteries, Sci. Adv. 7 (37) (2021) eabh3482.
[101] D. Meyer, H. Hoppeler, C. Gerber, Structure and contractile force of the supraspinatus muscle is correlated with the results of rotator cuff reconstruction, Orthop Proc 90-B (Supp II) (2008), 293-293.
[102] A. Fearon, J.E. Dahlstrom, J. Twin, et al., The Bonar score revisited: region of evaluation significantly influences the standardized assessment of tendon degeneration, J. Sci. Med. Sport 17 (4) (2014) 346–350.
[103] A. Boudaoud, A. Burian, D. Borowska-Wykret, et al., Fibriltool, an ImageJ plug-in to quantify fibrillar structures in raw microscopy images, Nat. Protoc. 9 (2) (2014) 457–463.